MOSFET Power Loss Estimation in *LLC* Resonant Converters: Time Interval Analysis

Ettore Scabeni Glitz, *Student Member, IEEE*, and Martin Ordonez, *Member, IEEE*

***Abstract*—In the past ten years, *LLC* resonant converters have become a mainstream topology for dc/dc power conversion, and multiple design tools have been developed for this topology, including controllers, regulators, soft-switching techniques, etc. While many tools are available for designing this converter, techniques for accurately determining power losses in the inverter MOSFETs of the topology based on time-domain analysis have not been fully explored yet. Precise power loss estimation is fundamental to determine the thermal behavior of the switches before the converter is built, which accelerates and optimizes the thermal management design process. In addition, accurate methods of estimating conduction losses, which are dominant in this topology, switching losses, and body diode losses are lacking in the literature. This paper proposes a method for enhancing power loss estimation in *LLC* inverter MOSFETs based on time-domain analysis of the converter. Moreover, a detailed characterization of MOSFET's conduction losses (P_{cond}), switching losses (P_{sw}), and body diode losses (P_{diode}), including the effects of different parameters such as gate-source voltage (V_{GS}), junction temperature (T_j), drain current (I_D), and drain-source voltage (V_{DS}), is presented, which can further improve power loss assessment in this topology. The developed method based on time interval analysis replaces the simplistic first-harmonic approximation (FHA), which allows for improved power loss calculations. Further improvement is obtained with the detailed characterization of the switching device. As verified by simulation and experimental results, the proposed estimation tool provides a significant boost in accuracy for power loss determination when compared to the existing method for power loss estimation using FHA.**

***Index Terms*—Design tool, device characterization, first-harmonic approximation (FHA), *LLC* resonant converter, MOSFET, power losses, time domain, time interval analysis (TIA).**

I. INTRODUCTION

When designing a power electronics converter, the determination of operating limitations, electrical component capabilities, and thermal management of active components require design tools which predict the behavior of the topology. Power loss determination, in particular, is essential for the design of an adequate thermal management, which guarantees appropriate operating temperatures, assuring the durability of the equipment and safety of the operator [1]. However, this assessment can be compromised by oversimplified prediction techniques, and by the limited information provided by datasheets regarding conduction (P_{cond}), switching (P_{sw}), and body diode losses (P_{diode}), which is often presented with reference to insufficient operating conditions. As a result, the final design may not dissipate power as predicted by the design tool, which will result in elevated temperatures, thus increasing leakages and compromising reliability [2].

The *LLC* resonant converter [3], [4] is a popular topology in power electronics, and many design tools have been developed for this converter, since it presents advantages which are of interest for applications such as electric vehicle battery charging [5]–[9], renewable energy systems [10]–[12], and diverse low-power applications [13]–[15]. Strategies for control [16]–[19], regulation [20], [21], and synchronous rectification driving schemes [22], [23] have been proposed in the literature, and design considerations for improved performance are also available [24]–[28]. However, there are still opportunities for exploring accurate power loss estimation techniques in *LLC* MOSFETs using time-domain expressions. Steady-state analysis of different parallel [29], [30], and series [31]–[33] resonant converter topologies have been investigated in the literature, including *LLC* resonant converters [27], [34]–[39]. However, these do not consider the impact of different loading conditions [34]–[36] or do not present time-domain equations which can be easily applied to different operating conditions and load configurations [37]–[41] for power loss assessment. The current established method for estimating time-domain behavior of *LLC* resonant converters consists of the First-Harmonic Approximation (FHA), which does not provide accurate results under certain operating conditions [42], thus providing poor power loss predictions [43].

One of the advantages presented by *LLC* resonant converters is the soft switching of the inverter MOSFETs, which produces smaller P_{sw} [44]. As a result, P_{cond} is dominant in this topology [45]. This loss mechanism is directly related to the ON-state resistance ($R_{\text{DS(on)}}$) of the switch, which is dependent on the gate-source voltage (V_{GS}), junction temperature (T_j), and drain current (I_D) [46]. Nevertheless, most models proposed in the literature for MOSFET power losses only take into account the dependence of this parameter with T_j, focusing on accurately determining the device's P_{sw} [47]–[49]. However, due to the operating characteristics of *LLC* resonant converters, accurately estimating P_{cond} by considering different values and polarities

Manuscript received November 30, 2018; revised February 15, 2019; accepted March 24, 2019. Date of publication April 8, 2019; date of current version September 6, 2019. This work was supported by the Natural Sciences and Engineering Research Council (NSERC). Recommended for publication by Associate Editor M. Harfman-Todorovic. *(Corresponding author: Martin Ordonez.)*

The authors are with the Department of Electrical and Computer Engineering, The University of British Columbia, Vancouver, BC V6T 1Z4, Canada (e-mail: ettoreglitz@ieee.org; mordonez@ieee.org).

Color versions of one or more of the figures in this paper are available online at http://ieeexplore.ieee.org.

Digital Object Identifier 10.1109/TPEL.2019.2909903

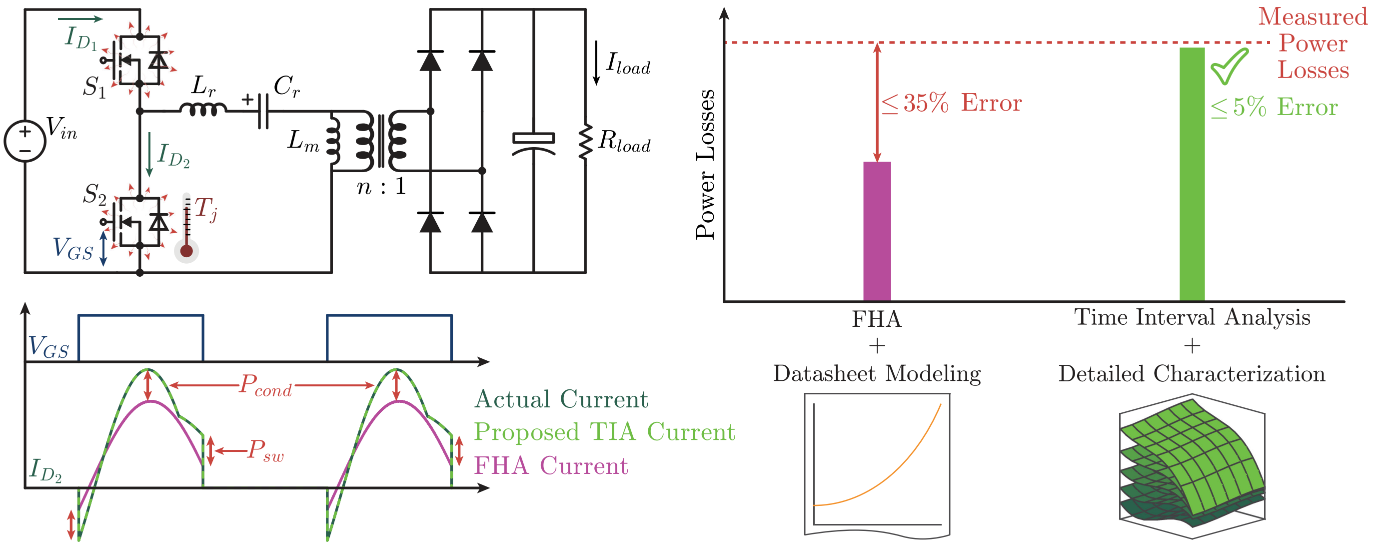

Fig. 1. *LLC* MOSFET power loss estimation: Large errors occur using first-harmonic approximation (FHA) (magenta). Switching, conduction, and body diode losses are determined with increased accuracy using the developed time-domain equations based on time interval analysis (TIA) in association with the proposed detailed characterization (green).

of I_D, T_j, and V_{GS} can help to further increase the precision of power loss estimation in the MOSFETs of the topology [43]. In addition, a detailed characterization of other loss mechanisms such as P_{sw} and P_{diode} are necessary for adequate loss estimation of the inverter MOSFETs. Moreover, since P_{cond}, P_{sw}, and P_{diode} are directly related to I_D, precise determination of the time-domain behavior of this parameter, considering different loading conditions and configurations, is essential.

This paper presents time-domain equations based on time interval analysis (TIA), a powerful tool for determining the behavior of *LLC* resonant converters under different operating conditions, as well as an improved power loss assessment for the switches of this topology. A better determination of I_D, when compared to the simplistic approximation from FHA, is obtained that not only allows for improved P_{cond} calculation, but also for the precise determination of parameters necessary for an appropriate assessment of P_{sw} and P_{diode}. Moreover, the presented detailed characterization of P_{cond}, P_{sw}, and P_{diode} as a prediction equation function of parameters such as V_{GS}, T_j, I_D, and drain-source voltage (V_{DS}) allows for enhanced power loss determination.

Fig. 1 outlines the proposed estimation tool versus the existing techniques. Power losses and electrical behavior of the converter are analyzed, and simulation and experimental results reveal significant improvements in accuracy for the determination of losses employing the described method versus FHA and datasheet modeling of switch parameters.

II. MOSFET POWER LOSS MODELING

As mentioned in the previous section, the detailed characterization of P_{cond}, P_{sw}, and P_{diode} under different operating conditions is recommended for the appropriate assessment of losses in *LLC* MOSFETs. In this topology, P_{cond} is dominant especially under heavy loading conditions, as shown in Fig. 2. Nevertheless, appropriate determination of P_{sw} and P_{diode} is necessary for the complete assessment of losses in the topology.

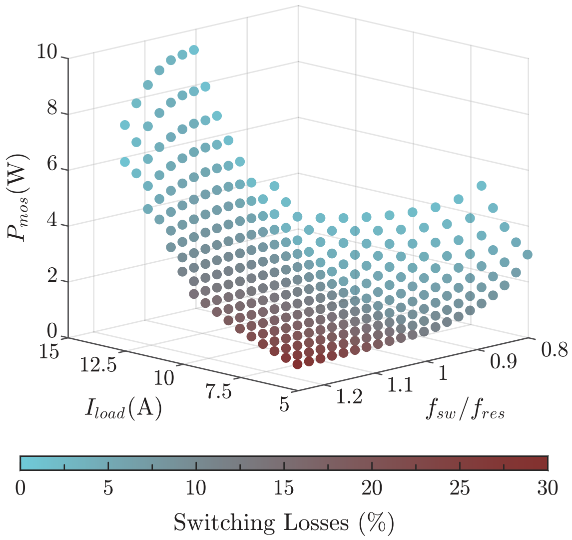

Fig. 2. Simulation of power losses in *LLC* MOSFETs for different operating conditions showing reduced contribution of switching losses, with predominant conduction losses.

A. Conduction Loss Characterization

In power MOSFETs, conduction losses are given by $P_{\mathrm{cond}} = R_{\mathrm{DS(on)}} I_D^2$. Datasheets often provide the dependence of $R_{\mathrm{DS(on)}}$ with T_j for selected values of I_D and V_{GS}, as shown in Fig. 3, even though it is known that $R_{\mathrm{DS(on)}}$ is a function of all three parameters. This lack of information leads

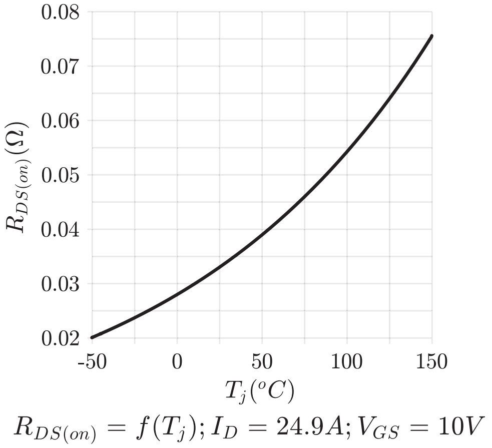

Fig. 3. MOSFET datasheet example (IPZ60R040C7) of $R_{\mathrm{DS(on)}}$ modeled as a function of T_j, not considering the impact of V_{GS} and I_D [50].

to inaccuracies in the determination of P_{cond} at conditions other than those specified by the document. In topologies such as the *LLC* resonant converter, I_D assumes different values during steady-state operation, as can be observed in Fig. 1, and various T_j and V_{GS} values must be accounted for. Therefore, a model for conduction losses that takes into account variations in V_{GS}, I_D, and T_j is a must for increased precision in the calculation of power losses in such a topology.

In order to improve power loss assessment, a detailed characterization of conduction losses was performed at the device level. A constant and known V_{GS} and different known values of I_D were applied to the device. Precision instruments were used to measure I_D, V_{GS}, and drain-source voltage (V_{DS}), and resistance temperature detectors (RTDs) were employed to assess case temperature (T_{case}), as shown in Fig. 4(a). The determination of T_j was performed by employing the thermal equivalent circuit of the device, shown in Fig. 4(b). From the circuit, it is possible to observe that $T_j = P_{\mathrm{mos}} R_{\mathrm{th_{jc}}} + T_{\mathrm{case}}$, where P_{mos} are the power losses in the MOSFET, determined from V_{DS} and I_D measurements, T_{case} is measured with RTDs, and $R_{\mathrm{th_{jc}}}$ is the thermal resistance between junction and case, which is considered to be constant. Subsequent changes in V_{GS} and T_j with the aid of a thermal chamber allowed for measurements at different operating conditions.

In order to optimize the determination of the polynomial expression for $R_{\mathrm{DS(on)}}$ as a function of V_{GS}, I_D, and T_j, design of experiments (DoE) can be employed to minimize the number of measurements required. In the presented case, 33 measurements were performed employing the simple test circuit shown in Fig. 4(a), in a process that can be easily automated. The obtained third-order expression for $R_{\mathrm{DS(on)}} = f(T_j, I_D, V_{\mathrm{GS}})$ translates into different families of operating surfaces, shown in Fig. 5.

In the obtained characterization, it was found that V_{GS} did not impact the value of $R_{\mathrm{DS(on)}}$ as significantly as did I_D and T_j for the considered range (from 8 to 14 V). The $R_{\mathrm{DS(on)}}$ increases for higher temperatures and positive values of I_D, as expected. For negative values of I_D, on the other hand, the obtained behavior is different, as shown in Fig. 5. The *LLC* resonant converter operates in this region during part of the steady-state cycle, and the adequate modeling of I_D, which is not contemplated by FHA, is essential for the precise determination of power losses in the MOSFETs of this topology under different operating conditions and load configurations.

B. *Switching Loss Characterization*

As mentioned in the previous sections, one of the advantages of *LLC* resonant converters is the soft switching of the inverter MOSFETs, which only suffer from turn-off losses. For this reason, the appropriate characterization of this loss mechanism is ideal for the precise determination of losses in this topology.

However, power loss assessment using electrical measurements in an operating converter is not adequate, since at high frequencies, EMI/RFI (electromagnetic interference/radio frequency interference) pose challenges to the measurement of electrical quantities [51]. Electrical measurements also introduce disturbances in the electrical behavior of the circuit, which compromise the quality of the power loss measurement. Thermal measurement with RTDs or thermocouples is also not possible since these rely on the measurement of electrical parameters for determining temperature. Therefore, calorimetric measurements for determining losses employing a thermal camera, as shown in Fig. 6, is a viable alternative. The relationship between T_{case} and P_{mos} is given by $T_{\mathrm{case}} = P_{\mathrm{mos}} R_{\mathrm{th_{ca}}} + T_{\mathrm{amb}}$, derived from the thermal equivalent circuit of the device shown in Fig. 4(b). The thermal resistance $R_{\mathrm{th_{ca}}}$ can be obtained by applying a constant known value of current through the device under test and measuring P_{mos} with precision instruments, as well as T_{case} and T_{amb} with a thermal camera, as shown in Fig. 6(a). By changing the applied current, it is possible to obtain different temperature and power levels, and a linear relationship between $T_{\mathrm{case}} - T_{\mathrm{amb}}$ and P_{mos} is obtained, as Fig. 6(b) shows. This allows for the determination of the power losses of a device based on its operating temperature, regardless of the frequency it operates, in a minimally invasive fashion. It is important to note that the operating conditions such as air flow and measurement positions must be maintained the same for the relationship to remain valid.

In order to characterize P_{sw}, three variables were considered in the analysis: V_{DS}, I_D, and T_j. While V_{GS} can also impact the value of the observed P_{sw}, this parameter was left unchanged and at the same levels that were used in the experimental measurements presented in Section V. The circuit employed for the characterization of the device can be observed in Fig. 7. The auxiliary switch S2 was employed to isolate the turn-off losses in the device under test (DUT) S1. As can be observed in Fig. 8, S2 was turned ON at α, which is a few nanoseconds before γ, which is when S1 is turned ON. By turning S2 ON, the voltage V_{DS} is reduced across both MOSFETs, since they are connected in parallel, even though the DUT S1 is still turned OFF. After V_{DS} is at a very low voltage, which occurs at β, the MOSFET S1 can

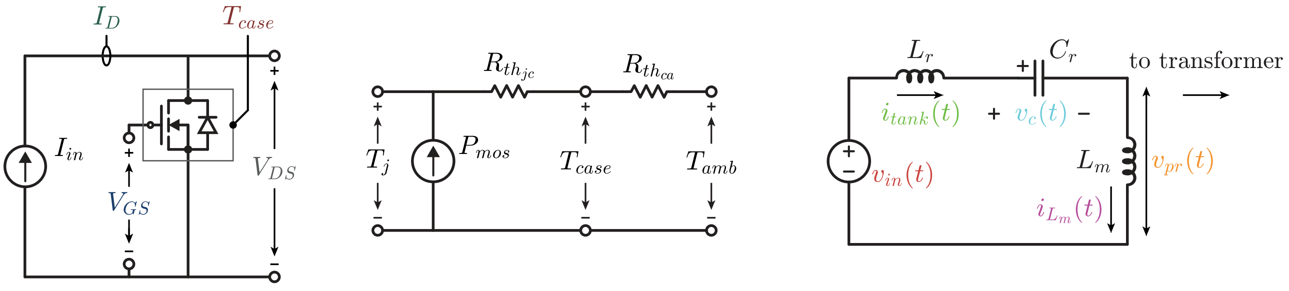

(a) (b) (c)

Fig. 4. (a) Circuit employed for developing the detailed model, (b) simplified thermal equivalent circuit of a MOSFET, and (c) equivalent circuit for the primary of the *LLC* resonant converter.

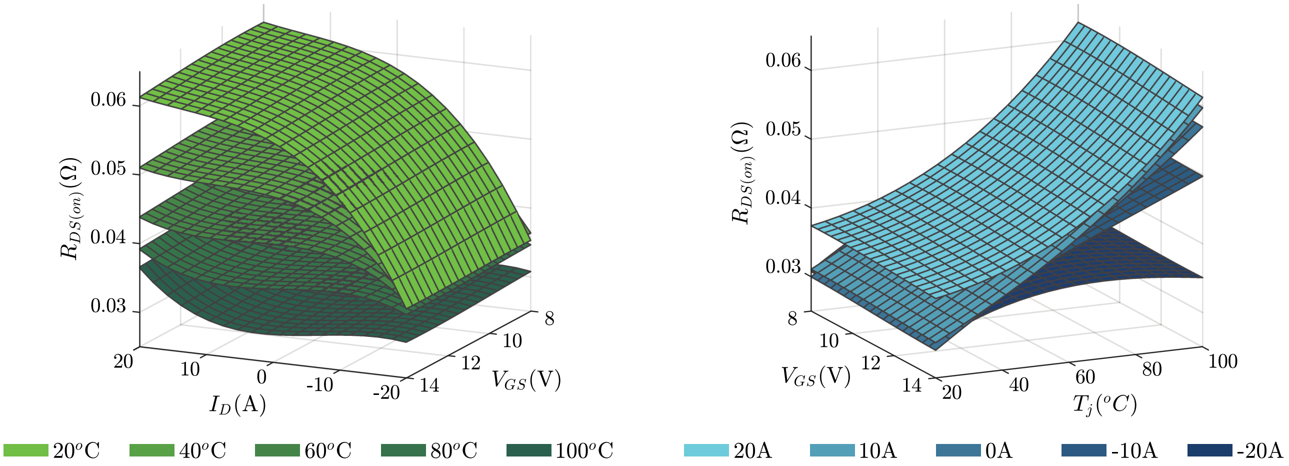

(a) (b)

Fig. 5. Operating surfaces of $R_{\mathrm{DS(on)}}$ in the detailed model showing considerable dependence on $R_{\mathrm{DS(on)}}$ with both T_j and I_D: (a) surfaces of $R_{\mathrm{DS(on)}}$ as a function of V_{GS} and I_D for different values of T_j and (b) surfaces of $R_{\mathrm{DS(on)}}$ as a function of V_{GS} and T_j for different values I_D. It is possible to observe that not only the magnitude, but also the polarity of I_D affects $R_{\mathrm{DS(on)}}$.

be turned ON. S1 is then turned ON at γ, and since V_{DS} is at a reduced value, this device turns ON with soft switching. S2 is then turned OFF at δ and S1 conducts for the majority of the ON-time. At turn OFF, represented by ϵ, the device S1 is subject to turn-off losses until the switching event is over at ζ. The waveforms of the gating signals V_{DS} and I_D can be observed in Fig. 8. DoE was once again employed for the determination of the testing conditions of the circuit and calorimetry was employed to determine the value of P_{mos} under every operating condition. Since the duty cycle (D) of the switch is known, P_{cond} can be extracted from P_{mos} and P_{sw} can be divided by the switching frequency f_{sw} so that the turn-off energy E_{off} can be obtained.

As a result, a third-order expression for $E_{\mathrm{off}} = f(T_j, I_D, V_{\mathrm{DS}})$ is obtained, which translates into different families of operating surfaces, shown in Fig. 9. It is possible to observe from the surfaces that the impact of T_j does not significantly impact the observed E_{off}, unlike what is observed in the case of the characterization of $R_{\mathrm{DS(on)}}$. As expected, an increase in I_D or V_{DS} represents higher turn-off energy values and increased P_{sw}. For the analysis of P_{sw} in the *LLC* resonant converter, the blocking voltage V_{DS} is the input voltage V_{in} and the turn-off drain current I_D can be determined based on time-domain expressions.

C. Body Diode Loss Characterization

For the inverter MOSFETs of the *LLC* resonant converter to operate with soft switching at turn-on, the body diodes of the device must conduct during the dead time, so as to reduce V_{DS} before the channel of the switch is formed. As a result, conduction losses in the body diode of the device originate because of the forward voltage drop V_{diode}. Thus, a detailed characterization of this parameter is also needed for the appropriate calculation of P_{mos}. The calculation process is similar to that performed for the characterization of $R_{\mathrm{DS(on)}}$, but the direction of the current shown in Fig. 4(a) is reversed, and the device is kept OFF at all times. Since V_{GS} does not play a role in this loss process, the impact of only I_D and T_j is considered in the characterization.

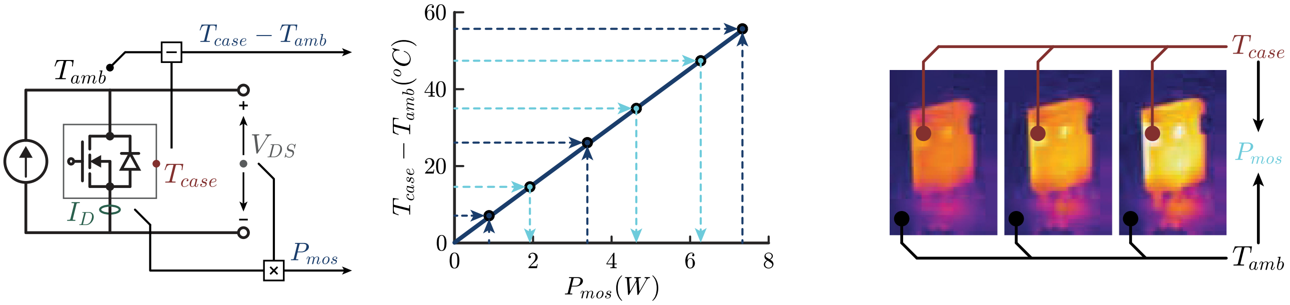

(a) (b) (c)

Fig. 6. Measurement of power losses is possible in high-frequency operation using calorimetry. (a) Calibration procedure, where dc power losses are measured alongside their respective temperature differences. (b) Linear relationship obtained between temperature difference and power losses, which can be used to determine P_{mos} based on (c) different temperature readings from a thermal camera.

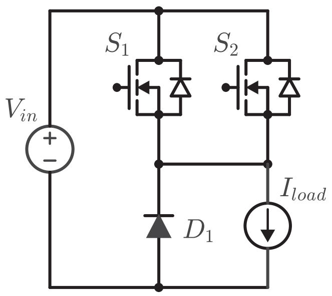

Fig. 7. Test circuit employed for the characterization of P_{sw}.

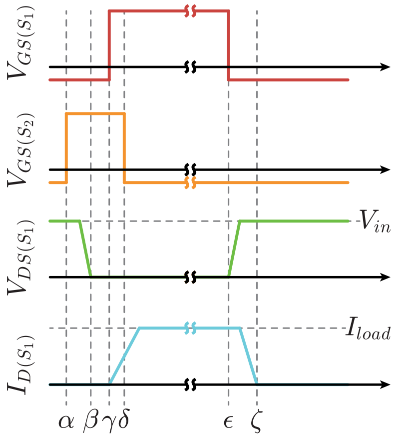

Fig. 8. Key waveforms used for the determination of E_{off}.

The result is a third-order expression for $V_{\text{diode}} = f(T_j, I_D)$, which translates into a single operating surface, shown in Fig. 10. As expected, higher values of T_j result in smaller V_{diode}, which is also observed at lower I_D levels.

This detailed characterization of V_{diode} allows for the determination of losses which result from the conduction of the body diode during dead time. Reverse recovery losses are not a concern as long as the operation of the converter is stable, proper dead times are considered, and the converter operates outside of the capacitive region [52], [53]. This is because the body diode will stop conducting as the channel is formed, and the drain current will instead circulate through the channel of the device.

III. TIME-DOMAIN EQUATIONS BASED ON TIA FOR *LLC* RESONANT CONVERTERS

Time-domain equations allow for the behavior of converters to be studied under different design parameters and operating conditions without the need for employing simulation software. This is especially useful when determining power losses in different topologies. Since the timescale for thermal phenomena is substantially different from that observed in electrical behavior, simulation must be carried out for a considerable amount of time with a significantly small time step before steady state is reached for both electrical and thermal properties, which can be a time-consuming process. Employing time-domain equations eliminates this problem, since the electrical behavior is already determined at steady state, and thermal characteristics can be easily assessed within a couple of iterations.

Precise time-domain equations for *LLC* resonant converters are required to determine power losses in the inverter MOSFETs employing a thermal model without using time-consuming simulation software. While FHA is the established method for determining the behavior of the converter, it oversimplifies the obtained waveforms to a degree that they are not useful for accurate power loss determination, since P_{cond} and P_{diode} determination will be imprecise due to the shape of the waveforms and P_{sw} will be calculated based on inaccurate values of turn-off currents. As an alternative, TIA allows for the determination of time-domain equations that reflect the actual behavior of the converter under different operating conditions, accounting for the non-sinusoidal characteristics of the waveforms of the converter. Consider the topology shown in Fig. 1. The circuit connected to the primary of the transformer can be represented by that shown in Fig. 4(c). Analysis of the capacitor voltage and inductor currents under different operating conditions allows for the determination of accurate time-domain equations for *LLC* resonant converters, which are necessary for the determination of MOSFET power losses.

A. Operation Above the Resonant Frequency

Fig. 11 shows the general behavior of the waveforms of the circuit shown in Fig. 4(c) when it operates above the resonant frequency, considering a duty cycle $D = 0.5$. Careful analysis

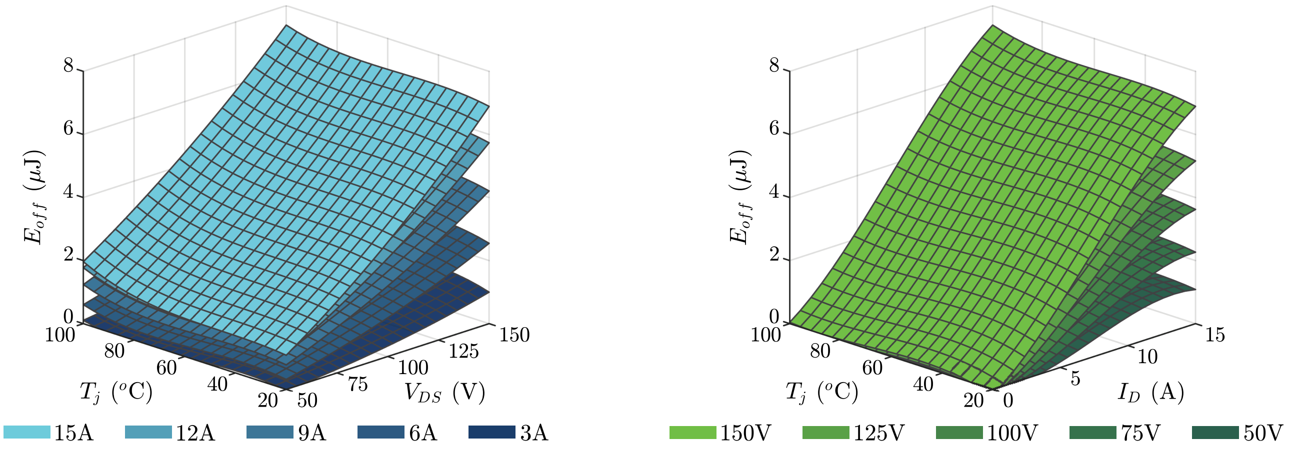

(a) (b)

Fig. 9. Operating surfaces of E_{off} in the developed characterization, showing considerable dependence with both V_{DS} and I_D: (a) surfaces of E_{off} as a function of V_{DS} and T_j for different values of I_D and (b) surfaces of E_{off} as a function of I_D and T_j for different values of V_{DS}. It is possible to observe that T_j does not affect losses significantly.

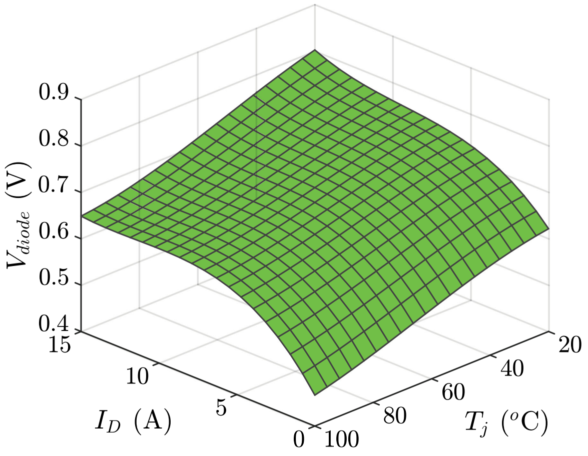

Fig. 10. Operating surface for V_{diode} as a function of I_D and T_j.

of $i_{\text{tank}}(t)$ reveals that it is not a purely sinusoidal waveform, so FHA will generate an oversimplified waveform that is not accurate for power loss estimation in the inverter MOSFETs; as demonstrated experimentally in Section V, the error generated by using FHA for power loss estimation can be as high as 35%.

It is possible to observe that the average value of $i_{\text{tank}}(t)$ and $i_{L_m}(t)$ is zero, and that the average value of $v_C(t)$ is $\frac{V_{\text{in}}}{2}$, assuming that $D = 0.5$. The moment the voltage source $v_{\text{in}}(t)$ assumes the value V_{in}, $t = t_0 = 0$. At this instant, the primary voltage of the transformer $v_{\text{pr}}(0)$ is $-nV_{\text{out}}$, which is maintained until $t = t_1$. At $t = t_1$, $v_{\text{pr}}(t_1) = nV_{\text{out}}$ and $v_{\text{in}}(t_1) = V_{\text{in}}$ until $t = \frac{1}{2f_{\text{sw}}}$, where f_{sw} is the switching frequency.

Therefore, analysis of the waveforms can be performed in two intervals: $t_0 = 0 < t < t_1$ and $t_1 < t < \frac{1}{2f_{\text{sw}}}$, where t_1 is defined as the time instant when the primary voltage of the transformer switches from $-nV_{\text{out}}$ to nV_{out}. During the first time interval, the time-domain equations of the circuit are determined as follows:

$$\begin{cases} v_C(t) = V_{\text{in}} + nV_{\text{out}} - L_r \frac{di_{\text{tank}}(t)}{dt} \\ i_{\text{tank}}(t) = C_r \frac{dv_C(t)}{dt} \\ -nV_{\text{out}} = L_m \frac{di_{L_m}(t)}{dt}. \end{cases} \tag{1}$$

If the initial conditions are $v_C(0) = V_0$, $i_{\text{tank}}(0) = I_0$, and $i_{L_m}(0) = I_{L_{m0}}$, the system of equations (1) can be rewritten as (3) shown at the bottom of the next page, where the superscript a indicates that these waveforms represent the behavior during the first interval, $t_0 = 0 < t < t_1$. During the second time interval $t_1 < t < \frac{1}{2f_{\text{sw}}}$, the time-domain equations of the circuit are as follows:

$$\begin{cases} v_C(t) = V_{\text{in}} - nV_{\text{out}} - L_r \frac{di_{\text{tank}}(t-t_1)}{dt} \\ i_{\text{tank}}(t) = C_r \frac{dv_C(t-t_1)}{dt} \\ nV_{\text{out}} = L_m \frac{di_{L_m}(t-t_1)}{dt}. \end{cases} \tag{2}$$

At the time $t = t_1$, $v_C(t_1) = V_1$, $i_{\text{tank}}(t_1) = I_1$, and $i_{L_m}(t_1) = I_{L_{m1}}$, the system of equations (2) can be rewritten as (4) shown at the bottom of the next page, where the superscript b indicates that these waveforms represent the behavior during the second interval, $t_1 < t < \frac{1}{2f_{\text{sw}}}$. For the time-domain equations to be solely functions of design parameters and known operating conditions, the unknown values $I_{L_{m1}}$, I_1, V_1, $I_{L_{m0}}$, I_0, V_0, and t_1 must be determined, as well as V_{in} or V_{out}, depending on which parameter is known. At $t = t_1$ the current flowing to the output of the circuit is zero, so $i_{L_m}(t_1) = I_{L_{m1}} = i_{\text{tank}}(t_1) = I_1$. This allows for the determination of an equation for $I_{L_{m0}}$. In addition, the average value of $I_{L_m}(t)$ is zero over a switching period. As a result, $I_{L_m}(0) = -i_{L_m}(\frac{1}{2f_{\text{sw}}})$, which allows for the determination of an equation for I_1.

Because inductor currents and capacitor voltages are state variables, $v_C^a(t_1) = v_C^b(t_1)$ and $i_{\text{tank}}^a(t_1) = i_{\text{tank}}^b(t_1)$. As a result, it is possible to obtain an equation for V_1 and I_0.

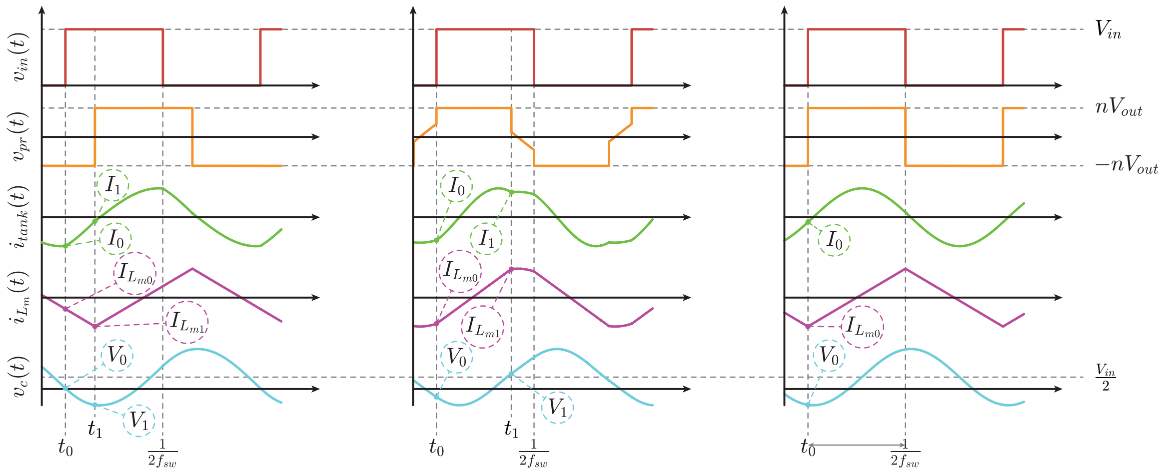

Above Resonance Below Resonance At Resonance

Fig. 11. Waveforms showing the general behavior of currents and voltages of the *LLC* resonant converter under different operating conditions.

Another property that can be explored is the average value of $v_C(t)$ and $i_{\text{tank}}(t)$. The average values of the inductor currents is zero for a switching period, so $i_{\text{tank}}(0) = -i_{\text{tank}}(\frac{1}{2f_{\text{sw}}})$. Since the average value of v_C is $\frac{V_{\text{in}}}{2}$ for a switching period, considering $D = 0.5$, $v_C(\frac{1}{2f_{\text{sw}}}) = -V_0 + V_{\text{in}}$. If the full-bridge topology is considered instead, then the average value of v_C is zero, and $v_C(\frac{1}{2f_{\text{sw}}}) = -V_0$. However, in this analysis the half-bridge topology shown in Fig. 1 will be considered. Using these properties allow for the determination of an equation for V_0 and an expression that relates V_{in} and V_{out}.

Once the expressions have been determined as functions of circuit parameters and operating conditions and simplified, the unknown parameters $I_{L_{m1}}$, I_1, V_1, $I_{L_{m0}}$, I_0, V_0, and V_{out} or V_{in} can be determined based on the established constraints

$$\begin{cases} v_C^a(t) = V_{\text{in}} + nV_{\text{out}} + I_0\sqrt{\frac{L_r}{C_r}}\sin\left(\frac{t}{\sqrt{L_rC_r}}\right) + (V_0 - V_{\text{in}} - nV_{\text{out}})\cos\left(\frac{t}{\sqrt{L_rC_r}}\right) \\ i_{\text{tank}}^a(t) = I_0\cos\left(\frac{t}{\sqrt{L_rC_r}}\right) - (V_0 - V_{\text{in}} - nV_{\text{out}})\sqrt{\frac{C_r}{L_r}}\sin\left(\frac{t}{\sqrt{L_rC_r}}\right) \\ i_{L_m}^a(t) = -\frac{nV_{\text{out}}t}{L_m} + I_{L_{m0}} \end{cases} \tag{3}$$

$$\begin{cases} v_C^b(t) = V_{\text{in}} - nV_{\text{out}} + I_1\sqrt{\frac{L_r}{C_r}}\sin\left(\frac{t-t_1}{\sqrt{L_rC_r}}\right) + (V_1 - V_{\text{in}} + nV_{\text{out}})\cos\left(\frac{t-t_1}{\sqrt{L_rC_r}}\right) \\ i_{\text{tank}}^b(t) = I_1\cos\left(\frac{t-t_1}{\sqrt{L_rC_r}}\right) - (V_1 - V_{\text{in}} + nV_{\text{out}})\sqrt{\frac{C_r}{L_r}}\sin\left(\frac{t-t_1}{\sqrt{L_rC_r}}\right) \\ i_{L_m}^b(t) = \frac{nV_{\text{out}}(t-t_1)}{L_m} + I_{L_{m1}} \end{cases} \tag{4}$$

$$\begin{cases} I_{L_{m1}} = I_1 = -\dfrac{nV_{\text{out}}}{4L_mf_{\text{sw}}} \\ V_1 = V_{\text{in}} - nV_{\text{out}} - \dfrac{V_{\text{in}} - 2nV_{\text{out}}\cos(A)}{2\cos(B)\cos(A-B)} - \dfrac{B}{m}nV_{\text{out}}\tan(A-B) \\ I_{L_{m0}} = \dfrac{nV_{\text{out}}}{4L_mf_{\text{sw}}}\left(\dfrac{A}{B} - 1\right) \\ I_0 = -\sqrt{\dfrac{C_r}{L_r}}\dfrac{2\dfrac{B}{m}nV_{\text{out}}\cos^2(B) + \sin(A)(2nV_{\text{out}}\cos(A-2B) + V_{\text{in}})}{2\cos(B)\cos(A-B)} \\ V_0 = V_{\text{in}} + nV_{\text{out}}(1 - 2\cos(A)) + \dfrac{\dfrac{B}{m}nV_{\text{out}}\sin(2B) + \cos(A)(2nV_{\text{out}}\cos(A) - V_{\text{in}})}{2\cos(B)\cos(A-B)} \\ \dfrac{V_{\text{out}}}{V_{\text{in}}} = -\dfrac{1}{2n}\dfrac{\sin(A-B)}{\dfrac{B}{m}\cos(B) + \sin(B)} \end{cases} \tag{5}$$

shown in (5) shown at the bottom of the previous page, where $A = \frac{t_1}{\sqrt{L_r C_r}}$, $B = \frac{1}{4 f_{\text{sw}} \sqrt{L_r C_r}}$, and m is the inductance ratio, defined as $m = \frac{L_m}{L_r}$. If both V_{in} and V_{out} are known, the unknown parameters can be calculated analytically from the equations presented. Otherwise, the loading condition needs to be provided so that t_1 can be determined numerically by assuming the conservation of energy

$$P_{\text{in}} = V_{\text{in}} f_{\text{sw}} \left(\int_0^{t_1} i^a_{\text{tank}}(t) dt + \int_{t_1}^{\frac{1}{2 f_{\text{sw}}}} i^b_{\text{tank}}(t) dt \right) = P_{\text{load}}. \tag{6}$$

Solving and simplifying (6) gives

$$P_{\text{in}} = 4 C_r f_{\text{sw}} V_{\text{in}}^2 \frac{\sin(A - B) \sin(\frac{A}{2} - B) \sin(\frac{A}{2})}{\frac{B}{m}(\cos(2B) + 1) + \sin(2B)} = P_{\text{load}}. \tag{7}$$

Additional power losses can be considered in (7) if the circuit is not assumed to be lossless. After t_1 has been determined numerically with (7), the remaining unknown parameters can be determined analytically with (5). This allows for the determination of the expressions for $i_{\text{tank}}(t)$ from (3) and (4), which are then used to derive the current $i_D(t)$ that flows through the inverter MOSFETs and generates power losses in the devices.

B. Operation Below the Resonant Frequency

The waveforms for operation of the converter under this condition are shown in Fig. 11. In this case, it clear that $i_{\text{tank}}(t)$ is not a sinusoidal waveform, thus, employing FHA would result in a poor approximation of MOSFET power losses. Instead, TIA can be employed to obtain detailed time-domain equations for the converter.

Once again, the average value of $i_{\text{tank}}(t)$ and $i_{L_m}(t)$ is zero, and the average value of $v_C(t)$ is $\frac{V_{\text{in}}}{2}$ if a duty cycle $D = 0.5$ is considered. The moment $v_{\text{in}}(t)$ assumes the value $V_{\text{in}}, t = t_0 = 0$. At this operating point, $v_{\text{pr}}(0) = nV_{\text{out}}$. At $t = t_1$, $v_{\text{pr}}(t)$ is no longer nV_{out}, but the voltage produced by i_{L_m}. During the second period of time, there is no current flowing to the output of the circuit, and $i_{L_m}(t) = i_{\text{tank}}(t)$. The input voltage remains at V_{in} until $t = \frac{1}{2 f_{\text{sw}}}$.

$$\begin{cases} v^a_C(t) = V_{\text{in}} - nV_{\text{out}} + I_0 \sqrt{\frac{L_r}{C_r}} \sin\left(\frac{t}{\sqrt{L_r C_r}}\right) + (V_0 - V_{\text{in}} + nV_{\text{out}}) \cos\left(\frac{t}{\sqrt{L_r C_r}}\right) \\ i^a_{\text{tank}}(t) = I_0 \cos\left(\frac{t}{\sqrt{L_r C_r}}\right) - (V_0 - V_{\text{in}} + nV_{\text{out}}) \sqrt{\frac{C_r}{L_r}} \sin\left(\frac{t}{\sqrt{L_r C_r}}\right) \\ i^a_{L_m}(t) = \frac{nV_{\text{out}} t}{L_m} + I_{L_{m0}} \end{cases} \tag{8}$$

$$\begin{cases} v^b_C(t) = V_{\text{in}} + I_1 \sqrt{\frac{L_r + L_m}{C_r}} \sin\left(\frac{t - t_1}{\sqrt{(L_r + L_m) C_r}}\right) + (V_1 - V_{\text{in}}) \cos\left(\frac{t - t_1}{\sqrt{(L_r + L_m) C_r}}\right) \\ i^b_{\text{tank}}(t) = I_1 \cos\left(\frac{t - t_1}{\sqrt{(L_r + L_m) C_r}}\right) - (V_1 - V_{\text{in}}) \sqrt{\frac{C_r}{(L_r + L_m)}} \sin\left(\frac{t - t_1}{\sqrt{(L_r + L_m) C_r}}\right) \\ i^b_{L_m}(t) = i^b_{\text{tank}}(t) \end{cases} \tag{9}$$

$$\begin{cases} I_{L_{m1}} = I_1 \\ I_{L_{m0}} = I_0 \\ I_1 = \sqrt{\dfrac{C_r}{L_r}} \dfrac{\dfrac{A}{m} nV_{\text{out}}(\cos(T) + \cos(A)) + \sin(A)(nV_{\text{out}}(1 + \cos(T)) - V_{\text{in}})}{\sqrt{m+1} \sin(T) \sin(A) - (\cos(T) - 1)(\cos(A) - 1)} \\ V_1 = V_{\text{in}} - nV_{\text{out}} + \dfrac{\dfrac{A}{m} nV_{\text{out}}(\sin(A) - \sqrt{m+1} \sin(T)) + (V_{\text{in}} - nV_{\text{out}}(\cos(T) + 1))(\cos(A) - 1)}{\sqrt{m+1} \sin(T) \sin(A) - (\cos(T) - 1)(\cos(A) - 1)} \\ I_0 = \sqrt{\dfrac{C_r}{L_r}} \dfrac{\dfrac{A}{m} nV_{\text{out}}(\cos(T) \cos(A) - \sqrt{m+1} \sin(T) \sin(A) + 1) + \sin(A)(nV_{\text{out}}(1 + \cos(T)) - V_{\text{in}})}{\sqrt{m+1} \sin(T) \sin(A) - (\cos(T) - 1)(\cos(A) - 1)} \\ V_0 = V_{\text{in}} - nV_{\text{out}} + \dfrac{\dfrac{A}{m} nV_{\text{out}}(\cos(T) \sin(A) + \sqrt{m+1} \sin(T) \cos(A)) + (V_{\text{in}} - nV_{\text{out}}(\cos(T) + 1))(\cos(A) - 1)}{(\cos(A) - 1)(\cos(T) - 1) - \sqrt{m+1} \sin(A) \sin(T)} \\ \dfrac{V_{\text{out}}}{V_{\text{in}}} = \dfrac{\dfrac{m}{An}}{\dfrac{2m}{A} + \cot(\dfrac{A}{2}) - \sqrt{m+1} \tan(\dfrac{T}{2})} \end{cases} \tag{10}$$

Therefore, the time-domain expressions that represent the operation of the converter below the resonant frequency are represented by (8) and (9) shown at the bottom of this page, where the superscript a indicates operation during the first time interval, from $t_0 = 0 < t < t_1$, and the superscript b indicates operation during the second time interval, from $t_1 < t < \frac{1}{2f_{\text{sw}}}$.

When $t = 0$, there is no current flowing to the secondary of the circuit, so $i_{L_m}(0) = I_{L_{m0}} = i_{\text{tank}}(0) = I_0$. The same situation occurs at $t = t_1$, so $i_{L_m}(t_1) = I_{L_{m1}} = i_{\text{tank}}(t_1) = I_1$. These properties allow for the determination of an expression for I_0.

Because inductor currents and capacitor voltages are state variables, $v_C^a(t_1) = v_C^b(t_1)$ and $i_{\text{tank}}^a(t_1) = i_{\text{tank}}^b(t_1)$. As a result, it is possible to obtain an equation for V_1 and I_1. Since the average value of $v_C(t)$ and $i_{\text{tank}}(t)$ is $\frac{V_{\text{in}}}{2}$ and zero, respectively, for a switching period, an equation for V_0 and an expression that relates V_{in} and V_{out} can be obtained.

Once the expressions have been determined as functions of circuit parameters and operating conditions and simplified, the unknown parameters $I_{L_{m1}}$, I_1, V_1, $I_{L_{m0}}$, I_0, V_0, and V_{out} or V_{in} can be determined based on the established constraints in (10) shown at the bottom of previous page, where $A = \frac{t_1}{\sqrt{L_r C_r}}$ and $T = \frac{\frac{1}{2f_{\text{sw}}} - t_1}{\sqrt{(L_r + L_m) C_r}}$. If both V_{in} and V_{out} are known, t_1 can be calculated numerically from the equations presented, and the remaining unknown parameters can be determined analytically. Otherwise, t_1 can be calculated numerically by applying the conservation of energy, using (6) with values for $i_{\text{tank}}(t)$ from (8) and (9). Because the resulting expression is rather extensive, it can be split into different sub-expressions, namely α, β and γ

$$P_{\text{in}} = C_r f_{\text{sw}} V_{\text{in}}^2 \frac{\alpha}{\gamma + \beta} = P_{\text{load}} \tag{11}$$

where α, β, and γ are defined in (13) shown at the bottom of this page. The development of the aforementioned equations which allow for the determination of the unknown parameters can be observed in the Appendix. After t_1 is determined with (11) and (13), the remaining unknown parameters from (10) can be determined analytically. This allows for the determination of the expressions for $i_{\text{tank}}(t)$ from (8) and (9), which are then used to determine the current $i_D(t)$ that flows through the MOSFETs and generates power losses in the device.

C. Operation at the Resonant Frequency

Waveforms for operation of the converter at the resonant frequency are shown in Fig. 11. Since the input and primary voltages are aligned, the circuit can be analyzed in its entirety during one time period, $t_0 = 0 < t < \frac{1}{2f_{\text{sw}}}$. TIA can be employed by considering that $v_C(0) = V_0$, $i_{\text{tank}}(0) = I_0$, and $i_{L_m}(0) = I_{L_{m0}}$ as shown in (14) shown at the bottom of this page.

The unknown parameters $I_{L_{m0}}$, I_0, V_0, and V_{in} or V_{out} must be determined for the equations that represent the circuit to be a function of known design parameters and operating conditions. At $t = t_0 = 0$, there is no current flowing to the output of the circuit, so $I_{L_{m0}} = I_0$. At resonance, the switching frequency f_{sw} is equal to the resonant frequency f_{res}, so $f_{\text{sw}} = f_{\text{res}} = \frac{1}{2\pi\sqrt{L_r C_r}}$. It is also known that $v_C(\frac{1}{2f_{\text{sw}}}) = -V_0 + V_{\text{in}}$. Since the average value of i_{L_m} is zero during a switching period, $I_{L_m}(\frac{1}{2f_{\text{sw}}}) = -i_{L_m}(0) = -I_0$. Conservation of energy can be used for the determination of the last unknown parameter with (6), where $i_{\text{tank}}^a(t) = i_{\text{tank}}^b(t) = i_{\text{tank}}(t)$ from (14). The unknown parameters $I_{L_{m0}}$, I_0, V_0, and V_{in} or V_{out} can be determined analytically based on the established constraints, and assuming that the converter provides an output power P_{load}

$$\begin{cases} I_{L_{m0}} = I_0 = -\frac{n V_{\text{out}} \pi \sqrt{L_r C_r}}{2 L_m} \\ V_0 = \frac{V_{\text{in}}}{2} - \pi \sqrt{\frac{L_r}{C_r}} \frac{P_{\text{load}}}{V_{\text{in}}} \\ \frac{V_{\text{out}}}{V_{\text{in}}} = \frac{1}{2n}. \end{cases} \tag{12}$$

After the unknown parameters have been determined with (12), the expression for $i_{\text{tank}}(t)$ from (14) can be determined as a function of known parameters and operating conditions. This allows for the determination of the current $i_D(t)$ that

$$\begin{cases} \alpha = \left(\sqrt{m+1} - \tan\left(\frac{T}{2}\right)\tan\left(\frac{A}{2}\right)\right)\left(\frac{A}{2}\cot\left(\frac{A}{2}\right) - 1\right) \\ \beta = \frac{A}{m}\left(\frac{\cos(A) + \cos(T) - 2\cos(A)\cos(T) - 2}{\sin(T)(\cos(A) - 1)} - \sqrt{m+1}\frac{\cos(A) + \cos(T) + 2\cos(A)\cos(T) + 2}{\sin(A)(\cos(T) + 1)}\right) \\ \gamma = \frac{1 + \frac{A}{2}\cot(\frac{A}{2}) + m}{\tan(\frac{A}{2})\tan(\frac{A}{2\sqrt{m+1}})} + \tan\left(\frac{T}{2}\right)\left(\tan\left(\frac{A}{2}\right) + A\right) - \sqrt{m+1}\left(2 + \frac{A}{2}\cot\left(\frac{A}{2}\right)\right) \end{cases} \tag{13}$$

$$\begin{cases} v_C(t) = V_{\text{in}} - nV_{\text{out}} + I_0\sqrt{\frac{L_r}{C_r}}\sin\left(\frac{t}{\sqrt{L_r C_r}}\right) + (V_0 - V_{\text{in}} + nV_{\text{out}})\cos\left(\frac{t}{\sqrt{L_r C_r}}\right) \\ i_{\text{tank}}(t) = I_0\cos\left(\frac{t}{\sqrt{L_r C_r}}\right) - (V_0 - V_{\text{in}} + nV_{\text{out}})\sqrt{\frac{C_r}{L_r}}\sin\left(\frac{t}{\sqrt{L_r C_r}}\right) \\ i_{L_m}(t) = \frac{nV_{\text{out}}t}{L_m} + I_{L_{m0}} \end{cases} \tag{14}$$

flows through the MOSFETs and generates power losses in the devices.

IV. *LLC* RESONANT CONVERTER POWER LOSS DETERMINATION AND ANALYSIS

The determination of equations based on the TIA for the *LLC* resonant converter allows for the time-domain analysis of this topology and improved power loss estimation when compared to the simplistic FHA. The obtained $i_{\text{tank}}(t)$ is of especial interest since this current flows through the MOSFETs of the topology shown in Fig. 1, generating power losses in these devices. The drain current of the top MOSFET $S1$ $i_{D_1}(t)$ is

$$\begin{cases} i_{D_1}(t) = i^a_{\text{tank}}(t), & \text{for } 0 < t < t_1 \\ i_{D_1}(t) = i^b_{\text{tank}}(t), & \text{for } t_1 < t < \frac{1}{2f_{\text{sw}}} \\ i_{D_1}(t) = 0, & \text{for } \frac{1}{2f_{\text{sw}}} < t < \frac{1}{f_{\text{sw}}}. \end{cases} \quad (15)$$

Conduction losses are predominant in this converter, especially at heavy loading conditions, as shown in Fig. 2. Therefore, an appropriate model for P_{cond}, such as the one developed in Section II, is recommended for increased accuracy in power loss determination. If a detailed characterization of $R_{\text{DS(on)}}$ is not performed, the limited information from the datasheet must be used instead, which may generate discrepancies in the determination of losses. Conduction losses can be obtained through integration

$$P_{\text{cond}} = f_{\text{sw}} \int_0^{\frac{1}{2f_{\text{sw}}}} i^2_{D_1}(t) R_{\text{DS(on)}} dt \quad (16)$$

where $i_{D_1}(t)$ is determined from (15), developed from the TIA equations as shown in Section III. Since $R_{\text{DS(on)}}$ depends on T_j, this parameter must be determined with iteration once all power loss mechanisms are accounted for.

Switching losses in this topology are restricted to turn-off losses as long as the converter operates outside of the capacitive region. This grants soft switching of the inverter MOSFETs during turn-on, which contributes to the efficiency of the converter. The turn-off current can be determined using the equations developed with TIA

$$i_{D_1(\text{off})} = i_D\left(\frac{1}{2f_{\text{sw}}}\right). \quad (17)$$

After this current has been determined, it is possible to employ the detailed characterization performed in Section II to determine E_{off}, where the value of V_{DS} is the blocking voltage of the device, which in this case is V_{in}, and T_j can be determined using iteration. The P_{sw} can then be determined by multiplying E_{off} by f_{sw}

$$P_{\text{sw}} = f_{\text{sw}} E_{\text{off}}(T_j, i_{D_1(\text{off})}, V_{\text{in}}). \quad (18)$$

If the detailed characterization of this power loss mechanism is not available, methods based on datasheet calculation of switching losses such as the one presented in [54] can be employed instead, even though inaccuracies may arise from this method.

The P_{diode} which occurs due to the conduction losses of the body diode during dead time can be determined provided that the detailed characterization of the forward voltage of the device V_{diode} is available

$$P_{\text{diode}} = f_{\text{sw}} \left(\int_{\frac{1}{2f_{\text{sw}}} - t_d}^{\frac{1}{2f_{\text{sw}}}} i_{D_1}(t) v_{\text{diode}} dt \right). \quad (19)$$

Information from the datasheet for V_{diode} can be used if the detailed characterization is not available, even though this process may result in inaccuracies. Since this parameter depends on T_j, iteration must be used after all power loss mechanisms have been accounted for.

Because of the intrinsic relationship between MOSFET power losses P_{mos} and junction temperature T_j, the operating temperature of the device and its power losses can be determined using iteration and considering the thermal equivalent circuit of MOSFETs shown in Fig. 4(b), which yields

$$T_j = T_{\text{amb}} + P_{\text{mos}}(R_{\text{th}_{\text{jc}}} + R_{\text{th}_{\text{ca}}}) \quad (20)$$

where $P_{\text{mos}} = P_{\text{cond}} + P_{\text{sw}} + P_{\text{diode}}$.

To better illustrate the procedure required for determining the inverter MOSFET power losses using TIA, a flowchart with the main decisions and processes involved is provided in Fig. 12.

In order to verify the effectiveness of TIA when compared to FHA, it is possible to estimate power losses employing the proposed method at different operating points, and compare with simulated MOSFET power losses. The same comparison can be performed using the established FHA versus simulated values. Fig. 13 shows that employing FHA results in unacceptably high levels of error at different operating points. The region where power losses are higher is of especial interest, since this is the condition for which adequate thermal management must be designed. Employing TIA, on the other hand, gives small values of error for all operating points of the circuit, and most importantly, gives adequate power loss prediction at higher power loss levels.

For the considered operating points shown in Fig. 13, an average error of 0.22% for power loss estimation was obtained when using TIA, with more than 97% of the calculations presenting an error smaller than 2%. FHA, on the other hand, presented an average error of 10.7%, with errors of up to 60% in some operating conditions. Thus, it is clear that the current approach of using FHA cannot properly estimate the behavior of *LLC* resonant converters and the expected power losses of *LLC* MOSFETs.

V. MODEL VALIDATION

In order to ensure that TIA reflects the time-domain behavior observed in a real converter, it is possible to compare the experimental results to calculated waveforms. An experimental prototype was built with the parameters listed in Table I. Fig. 14 shows oscilloscope captures of $v_{\text{in}}(t)$, $v_{\text{pr}}(t)$, $i_{\text{tank}}(t)$, and $i_{D_1}(t)$ for operation of the converter above the resonant frequency. It is possible to observe that the shape of the waveforms obtained with TIA closely correlate to those observed in the experimental results presented. In addition, the magnitude of the waveforms calculated using the developed method match those observed by

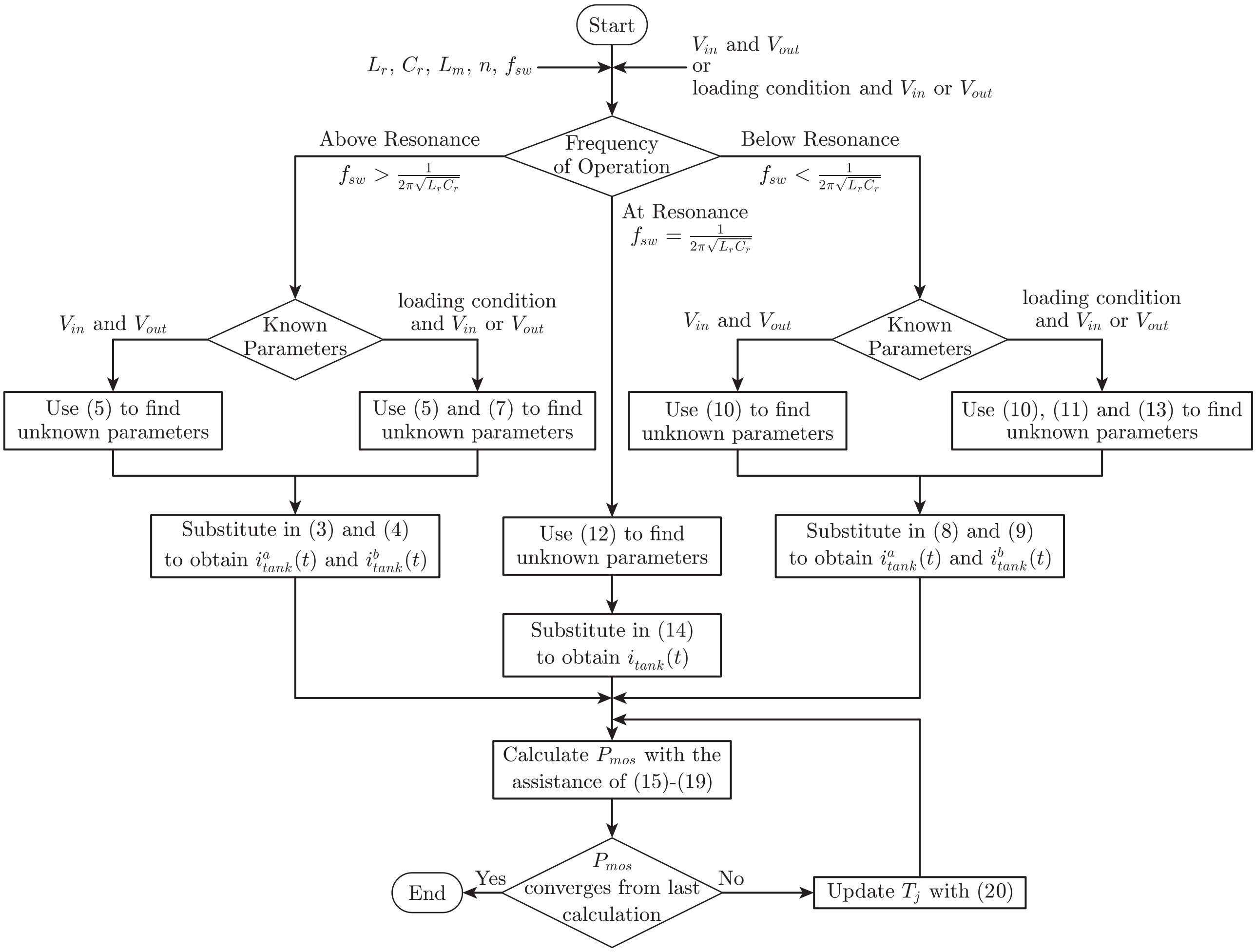

Fig. 12. Flowchart illustrating the main decisions and processes involved for determining *LLC* MOSFET power losses using TIA.

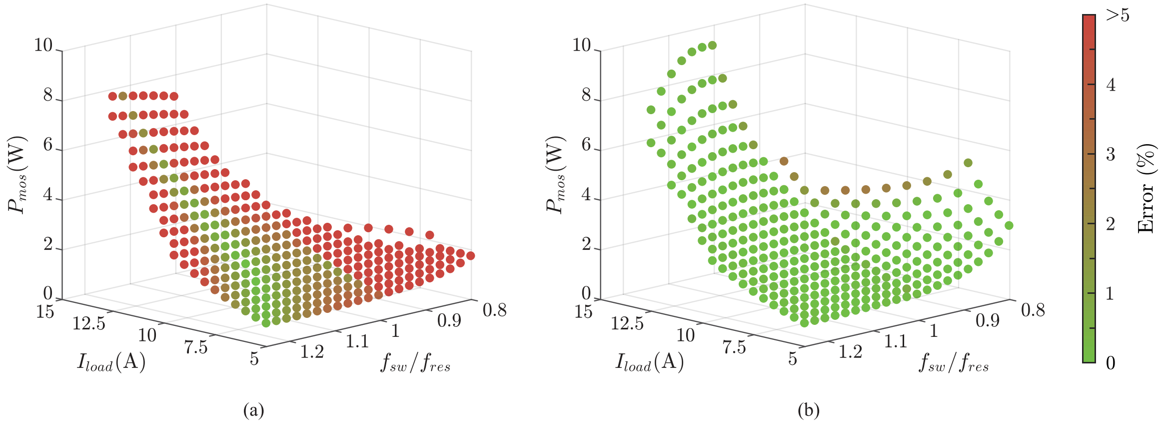

(a)

(b)

Fig. 13. Power loss estimation using (a) existing FHA + datasheet with estimation errors greater than 5% in most regions and (b) proposed TIA + detailed $R_{\mathrm{DS(on)}}$ with errors under 2% in most operating conditions.

TABLE I
LLC DESIGN PARAMETERS FOR P_{LOSS} ANALYSIS IN INVERTER MOSFETS

Parameter	Input Voltage V_{in}	Nominal Power P_{nom}	Nominal Load Current I_{nom}
Value	100 V	500 W	10 A
Parameter	Magnetizing Inductance L_m	Resonant Inductance L_r	Resonant Capacitance C_r
Value	19.7 μH	15.2 μH	192 nF
Parameter	Resonant Frequency f_{res}	Switching Frequency f_{sw}	Transformer Turns Ratio n
Value	93 kHz	80-120 kHz	1

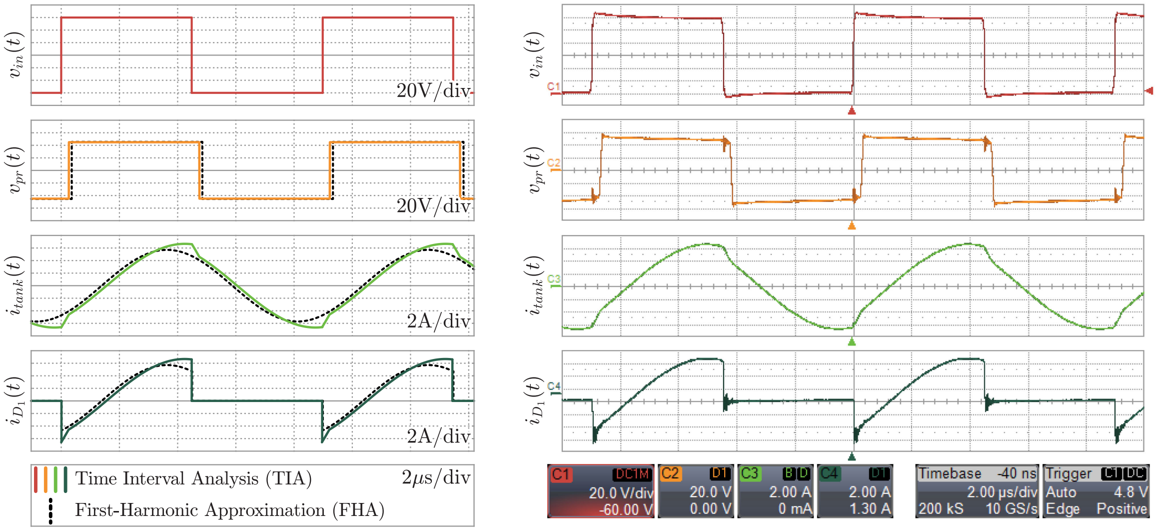

(a)

(b)

Fig. 14. Theoretical waveforms versus experimentation: (a) waveforms calculated using TIA and FHA and (b) actual experimental waveforms of $v_{\text{in}}(t)$ (red), $v_{\text{pr}}(t)$ (orange), $i_{\text{tank}}(t)$ (light green), and $i_{D_1}(t)$ (dark green) for the operation of the converter above the resonant frequency. Unlike FHA, the TIA waveforms follow the actual experimental waveforms with better accuracy.

the oscilloscope measurements. FHA, on the other hand, generates a prediction waveform that is oversimplified, with incorrect shapes and magnitude values. Because P_{mos} assessment depends on the accurate determination of the i_D which flows through the inverting MOSFETs, TIA is presented as an alternative to the oversimplified FHA.

Operation below the resonant frequency is shown in Fig. 15. Similar to the situation presented for operation above f_{res}, it is clear that the oversimplification imposed by FHA results in a waveform that cannot be used for power loss estimation. In this case, $i_{\text{tank}}(t)$ as provided by FHA presents a significant discrepancy regarding magnitude and shape when compared to experimental measurements and calculation using TIA. This not only affects the calculation of P_{cond}, but also greatly impacts the determination of turn-on and turn-off currents, as can be seen in the waveforms shown for $i_{D_1}(t)$, affecting switching loss assessment. Operation at f_{res}, as shown in Fig. 16, is also affected by the oversimplification imposed by FHA; while the shape of the waveforms obtained using both methods is similar, the calculated magnitude using FHA is incorrect when compared to that observed in experimental measurements or using TIA, which in turn yields good results.

In order to determine the P_{mos} of the inverter MOSFETs of the *LLC* resonant converter, the calorimetric method was employed in a similar fashion to that presented in Section II. First, the relationship between measured temperatures using a thermal camera and power losses using precision instruments was established. Next, by operating the *LLC* resonant converter under different conditions, and measuring T_{case} and T_{amb} with a thermal camera, it was possible to determine the power losses of the MOSFETs of the topology. Comparison between measurements and calculated values employing the detailed characterization of $R_{\text{DS(on)}}$, E_{off}, and V_{diode} with TIA suggests that it produces more reliable power loss predictions, with less than 5% error between P_{mos} prediction and experimental measurements. Power loss assessment using TIA and the datasheet modeling of P_{cond}, P_{sw}, and

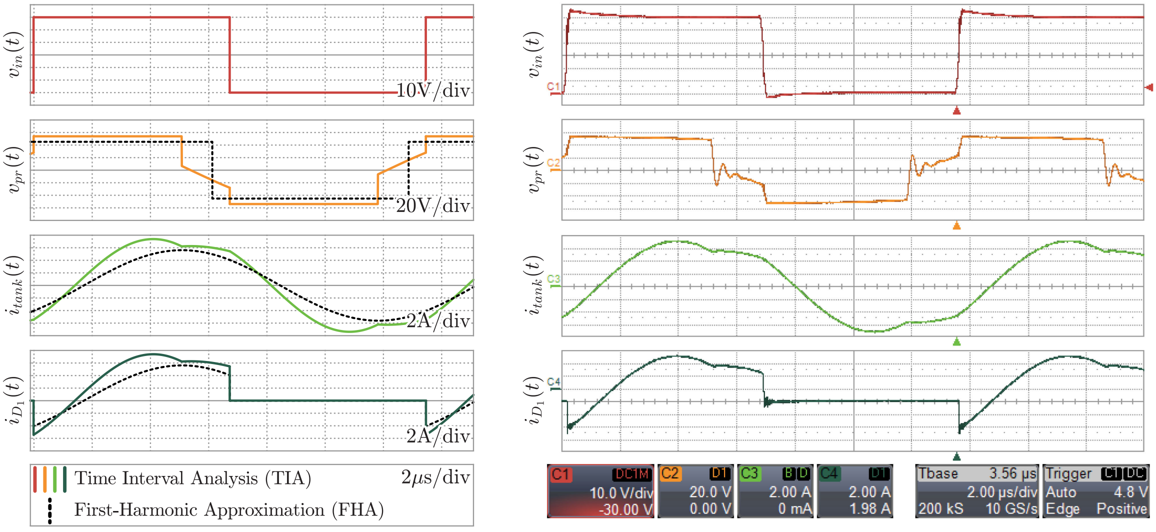

(a) (b)

Fig. 15. Theoretical waveforms versus experimentation: (a) waveforms calculated using TIA and FHA and (b) actual experimental waveforms of $v_{\text{in}}(t)$ (red), $v_{\text{pr}}(t)$ (orange), $i_{\text{tank}}(t)$ (light green), and $i_{D_1}(t)$ (dark green) for the operation of the converter below the resonant frequency. FHA produces a waveform that is substantially different and oversimplified from that obtained with TIA and in experimental measurements.

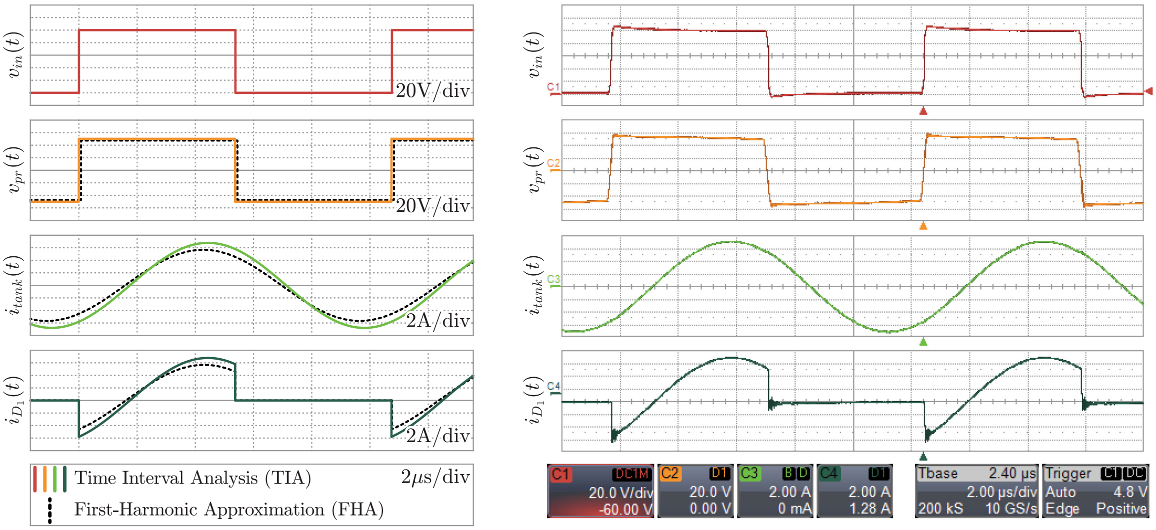

(a) (b)

Fig. 16. Theoretical waveforms versus experimentation: (a) waveforms calculated using TIA and FHA and (b) actual experimental waveforms of $v_{\text{in}}(t)$ (red), $v_{\text{pr}}(t)$ (orange), $i_{\text{tank}}(t)$ (light green), and $i_{D_1}(t)$ (dark green) for operation of the converter at the resonant frequency. Phase shift and amplitude error can be observed in the waveform generated with FHA, while the measured waveform coincides with that obtained with TIA.

P_{diode} was also considered. While it produces reliable results at certain operating conditions, the maximum error observed between P_{mos} calculation and measurement was almost 10%. In fact, the average error observed was reduced from 4.6% using datasheet modeling, to 2.7% using the detailed characterization presented. The third scenario consisted of using FHA to determine the drain current of the device and datasheet modeling of the device. This alternative resulted in errors of up to 35% for power loss assessment when compared to the experimental measurements, with an average error of 20%. Select measurements and calculations are shown in Fig. 17 for comparison, and it is possible to observe that using FHA always results in a high error for power loss determination, even when the converter operates at the resonant frequency. The measured power losses were obtained employing calorimetry, and the converter was set to operate either at constant P_{load} or at constant current mode, where $P_{\text{load}} = I_{\text{load}} V_{\text{out}}$.

It is also possible to observe that P_{cond}, P_{sw}, and P_{diode} are indicated graphically, and as observed in Fig. 2, P_{cond} represents the largest source of losses in the device. Considering the measured operating conditions, the contribution of P_{cond} accounted for an average of 86.8% of the total P_{mos} observed in the device. P_{sw} was responsible for an average of 8.5% of observed losses and P_{diode} for 4.7% on average.

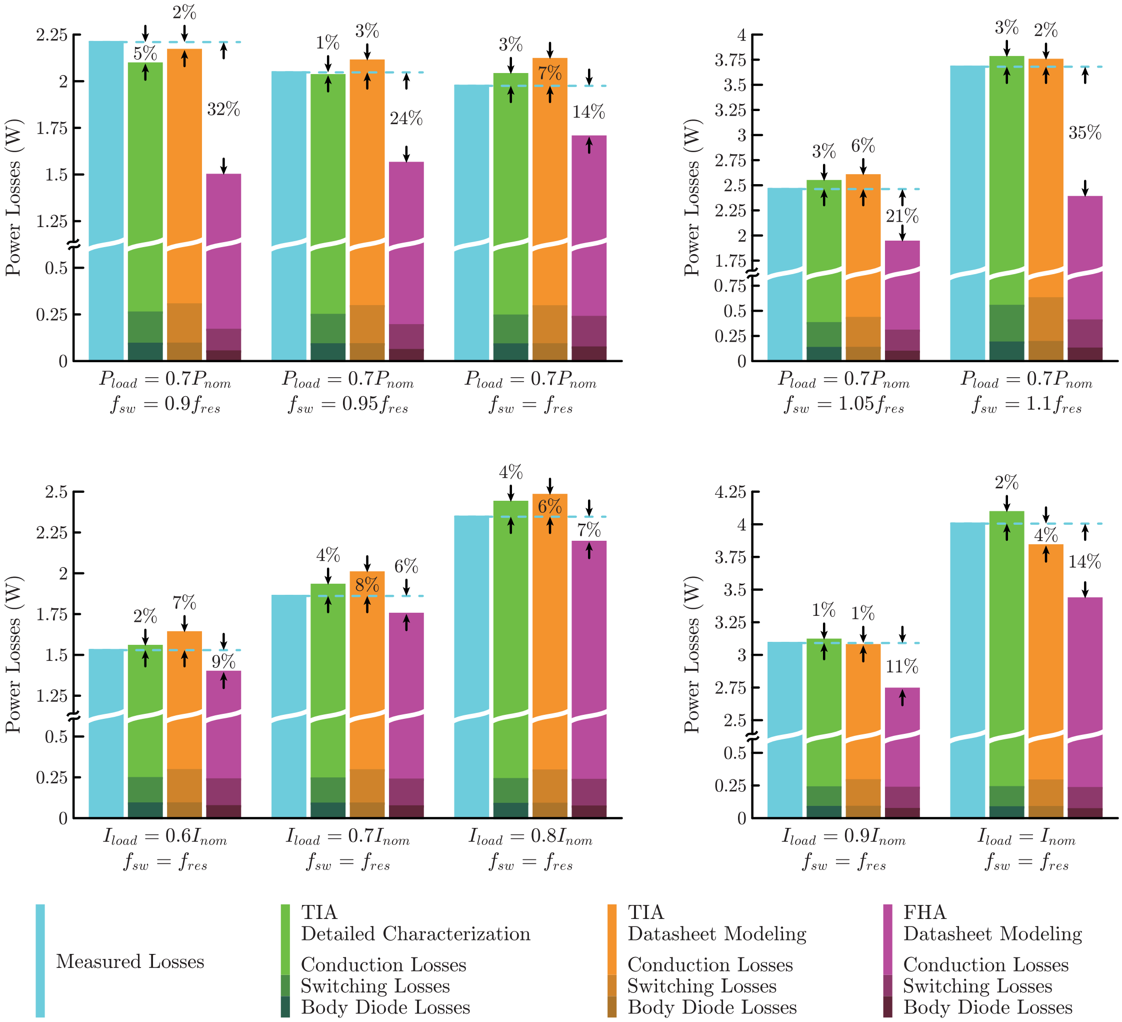

Fig. 17. Experimental versus calculated error: blue bars show the actual measured losses, green bars depict TIA technique with detailed characterization of the switch (good accuracy), orange bars represent TIA with datasheet $R_{\mathrm{DS(on)}}$ (average accuracy), and magenta shows FHA (excessive error). Improved accuracy is achieved with the appropriate determination of $i_D(t)$.

VI. CONCLUSION

This paper presented a new estimation tool for determining power losses in *LLC* MOSFETs before the resonant converter is built. Time-domain equations that describe the behavior of the topology based on operating conditions and design parameters were developed, and were able to produce waveforms that comply with simulated and experimental measurements. In addition, a detailed characterization of the MOSFET's on-state resistance ($R_{\mathrm{DS(on)}}$), turn-off energy (E_{off}), and forward diode voltage drop (V_{diode}) that considers the peculiarities observed with changes in gate-source voltage (V_{GS}), drain-source voltage (V_{DS}), junction temperature (T_j), and different values and polarities of drain current (I_D) was developed. This characterization increases the precision with which conduction losses (P_{cond}), switching losses (P_{sw}), and body diode losses (P_{diode}) are determined, thus improving the accuracy of the determination of total power losses in the switch (P_{mos}).

Steady-state time-domain equations based on TIA were able to better predict the behavior of the converter when compared to the existing method that employs the oversimplified FHA, as observed in simulation and experimental measurements. The developed method allows for not only an improved calculation of P_{cond}, but also for the appropriate determination of turn-off currents, necessary for the precise assessment of switching losses (P_{sw}).

The estimation tool was able to determine P_{mos} under different operating conditions with an average error of 0.22% when compared to simulation results, versus an error of up to 60% observed when employing FHA. Experimental measurements verified that TIA was able to determine *LLC* MOSFET losses with increased accuracy of less than 10% error, when compared to up to 35% error observed using FHA. When the detailed characterization of the device is employed for the determination of P_{mos}, the maximum error observed was reduced to 5%. Such considerable improvement results in faster and cheaper prototype design for power converters.

APPENDIX

A brief derivation of (10)–(13) is provided to facilitate the comprehension of the developed equations. Considering (8) and

(9), as well as the operating conditions outlined in Section III, the unknown parameters I_0, I_1, V_0, V_1, $I_{L_{m0}}$, $I_{L_{m1}}$, and t_1 must be determined. In addition, the value of both V_{in} or V_{out} may not be known for certain operating conditions. In order to determine the value of the unknown parameters, certain electrical properties of the circuit must be considered.

First, it is known that at $t = t_1$ there is no current flowing to the transformer connected to the primary of the circuit, so $i_{\text{tank}}(t_1) = i_{L_m}(t_1) = I_1 = I_{L_{m1}}$. In addition, there is no current flowing to the secondary of the circuit at $t = 0$. As a result, $i_{\text{tank}}(0) = i_{L_m}(0) = I_0 = I_{L_{m0}}$. This implies that at $t = t_1$, $i^a_{L_m}(t)$ from (8) becomes

$$I_0 = I_1 - \frac{nV_{\text{out}}t_1}{L_m}. \tag{21}$$

Because the voltage in the series resonant capacitor cannot change instantaneously, $v^a_C(t_1)$ from (8) must be equal to $v^b_C(t_1)$ from (9). That is

$$\begin{aligned} V_1 = V_{\text{in}} - nV_{\text{out}} + I_0\sqrt{\frac{L_r}{C_r}}\sin\left(\frac{t_1}{\sqrt{L_rC_r}}\right) \\ + (V_0 - V_{\text{in}} + nV_{\text{out}})\cos\left(\frac{t_1}{\sqrt{L_rC_r}}\right). \end{aligned} \tag{22}$$

Replacing I_0 from (21) into (22), and assuming that $A = \frac{t_1}{\sqrt{L_rC_r}}$ gives

$$\begin{aligned} V_1 = V_{\text{in}} - nV_{\text{out}} + \left(I_1 - \frac{nV_{\text{out}}t_1}{L_m}\right)\sqrt{\frac{L_r}{C_r}}\sin(A) \\ + (V_0 - V_{\text{in}} + nV_{\text{out}})\cos(A). \end{aligned} \tag{23}$$

Similarly, the tank current cannot change suddenly because of the resonant inductance, so $i^a_{\text{tank}}(t_1)$ from (8) must be equal to $i^b_{\text{tank}}(t_1)$ from (9). That is

$$\begin{aligned} I_1 = I_0\cos\left(\frac{t_1}{\sqrt{L_rC_r}}\right) \\ - (V_0 - V_{\text{in}} + nV_{\text{out}})\sqrt{\frac{C_r}{L_r}}\sin\left(\frac{t_1}{\sqrt{L_rC_r}}\right). \end{aligned} \tag{24}$$

Replacing I_0 from (21) into (24), and assuming that $A = \frac{t_1}{\sqrt{L_rC_r}}$ gives

$$\begin{aligned} I_1 = -\frac{nV_{\text{out}}t_1\cos(A)}{L_m(1-\cos(A))} \\ - (V_0 - V_{\text{in}} + nV_{\text{out}})\sqrt{\frac{C_r}{L_r}}\cot\left(\frac{A}{2}\right). \end{aligned} \tag{25}$$

Replacing I_1 from (25) into (21) and (23) gives

$$\begin{aligned} I_0 = -\frac{nV_{\text{out}}t_1}{L_m(1-\cos(A))} \\ - (V_0 - V_{\text{in}} + nV_{\text{out}})\sqrt{\frac{C_r}{L_r}}\cot\left(\frac{A}{2}\right) \end{aligned} \tag{26}$$

$$V_1 = 2V_{\text{in}} - 2nV_{\text{out}} - V_0 - \sqrt{\frac{L_r}{C_r}}\frac{nV_{\text{out}}t_1\cot\left(\frac{A}{2}\right)}{L_m}. \tag{27}$$

Another property that can be explored is related to $v_C(t)$. Because the topology being considered consists of the half-bridge inverter, and since a duty cycle $D = 0.5$ is assumed, $v^b_C(\frac{1}{2f_{\text{sw}}}) = -V_0 + V_{\text{in}}$. This property can be visualized in Fig. 11 and through the simulation of the circuit. Equating $v^b_C(\frac{1}{2f_{\text{sw}}})$ from (9) to $-V_0 + V_{\text{in}}$ gives (29).

Replacing I_1 from (25), V_1 from (27), considering that $A = \frac{t_1}{\sqrt{L_rC_r}}$ and $T = \frac{\frac{1}{2f_{\text{sw}}} - t_1}{\sqrt{(L_r+L_m)C_r}}$, and simplifying the resulting (30) shown at the bottom of this page.

Replacing V_0 from (30) into (25)–(27) gives (32)–(34) shown at the top of the next page.

In order to obtain the relationship between input and output voltage, it is possible to explore a characteristic of the current that flows through the resonant tank $i_{\text{tank}}(t)$; when $t = \frac{1}{2f_{\text{sw}}}$, $i^b_{\text{tank}}(\frac{1}{2f_{\text{sw}}}) = -I_0$, since the average current of the inductor is zero within a switching cycle. Therefore, (33) can be obtained.

Replacing I_0 from (33), I_1 from (32), V_1 from (34), considering that $A = \frac{t_1}{\sqrt{L_rC_r}}$ and $T = \frac{\frac{1}{2f_{\text{sw}}} - t_1}{\sqrt{(L_r+L_m)C_r}}$, and simplifying the resulting equation gives

$$\frac{V_{\text{out}}}{V_{\text{in}}} = \frac{\frac{m}{A}}{\frac{2m}{n} + \cot(\frac{A}{2}) - \sqrt{m+1}\tan(\frac{T}{2})} \tag{28}$$

$$\begin{aligned} -V_0 = I_1\sqrt{\frac{L_r + L_m}{C_r}}\sin\left(\frac{\frac{1}{2f_s} - t_1}{\sqrt{(L_r + L_m)C_r}}\right) \\ + (V_1 - V_{\text{in}})\cos\left(\frac{\frac{1}{2f_{\text{sw}}} - t_1}{\sqrt{(L_r + L_m)C_r}}\right). \end{aligned} \tag{29}$$

Together, the equations for I_1 and $I_{L_{m1}}$ from (32), V_1 from (34), I_0 and $I_{L_{m0}}$ from (33), V_0 from (30), and the relationship between V_{in} and V_{out} from (28) result in the system of equations presented in (10). If both V_{in} and V_{out} are known, t_1 can be calculated from the equations presented in (10). Otherwise, the conservation of energy can be used to determine this last unknown parameter—the input energy, found using the time-domain equations developed, is equal to the output power being delivered to the load, which is a required parameter to determine the unknown variables. This last equation can be determined as follows:

$$\begin{aligned} P_{\text{in}} = V_{\text{in}}f_{\text{sw}}\Bigg[\int_0^{t_1} i^a_{\text{tank}}(t)dt \\ + \int_{t_1}^{\frac{1}{2f_{\text{sw}}}} i^b_{\text{tank}}(t)dt\Bigg] = P_{\text{load}}. \end{aligned} \tag{31}$$

It is important to notice that P_{load} can be expressed in terms of $I_{\text{out}}V_{\text{out}}$, which grants greater flexibility in the calculation of the time-domain expressions. Solving (31) and replacing the

$$V_0 = V_{\text{in}} - nV_{\text{out}} + \frac{\frac{A}{m}nV_{\text{out}}(\cos(T)\sin(A) + \sqrt{m+1}\sin(T)\cos(A)) + (V_{\text{in}} - nV_{\text{out}}(\cos(T)+1))(\cos(A)-1)}{(\cos(A)-1)(\cos(T)-1) - \sqrt{m+1}\sin(A)\sin(T)} \tag{30}$$

$$I_{L_{m1}} = I_1 = \sqrt{\frac{C_r}{L_r}}\frac{\frac{A}{m}nV_{\text{out}}(\cos(T)+\cos(A))+\sin(A)(nV_{\text{out}}(1+\cos(T))-V_{\text{in}})}{\sqrt{m+1}\sin(T)\sin(A)-(\cos(T)-1)(\cos(A)-1)} \tag{32}$$

$$I_{L_{m0}} = I_0 = \sqrt{\frac{C_r}{L_r}}\frac{\frac{A}{m}nV_{\text{out}}(\cos(T)\cos(A)-\sqrt{m+1}\sin(T)\sin(A)+1)+\sin(A)(nV_{\text{out}}(1+\cos(T))-V_{\text{in}})}{\sqrt{m+1}\sin(T)\sin(A)-(\cos(T)-1)(\cos(A)-1)} \tag{33}$$

$$V_1 = V_{\text{in}} - nV_{\text{out}} + \frac{\frac{A}{m}nV_{\text{out}}(\sin(A)-\sqrt{m+1}\sin(T))+(V_{\text{in}}-nV_{\text{out}}(\cos(T)+1))(\cos(A)-1)}{\sqrt{m+1}\sin(T)\sin(A)-(\cos(T)-1)(\cos(A)-1)} \tag{34}$$

$$-I_0 = I_1\cos\left(\frac{\frac{1}{2f_{\text{sw}}}-t_1}{\sqrt{(L_r+L_m)C_r}}\right)-(V_1-V_{\text{in}})\sqrt{\frac{C_r}{(L_r+L_m)}}\sin\left(\frac{\frac{1}{2f_{\text{sw}}}-t_1}{\sqrt{(L_r+L_m)C_r}}\right) \tag{35}$$

$$\begin{aligned}P_{\text{in}} = C_r f_{\text{sw}} V_{\text{in}}^2 &\left(\sqrt{m+1}-\tan\left(\frac{T}{2}\right)\tan\left(\frac{A}{2}\right)\right)\left(\frac{A}{2}\cot\left(\frac{A}{2}\right)-1\right)\left(\frac{A}{m}\left(\frac{\cos(A)+\cos(T)-2\cos(A)\cos(T)-2}{\sin(T)(\cos(A)-1)}\right.\right.\\ &\left.-\sqrt{m+1}\frac{\cos(A)+\cos(T)+2\cos(A)\cos(T)+2}{\sin(A)(\cos(T)+1)}\right)+\frac{1+\frac{A}{2}\cot(\frac{A}{2})+m}{\tan(\frac{A}{2})\tan(\frac{A}{2\sqrt{m+1}})}+\tan\left(\frac{T}{2}\right)\left(\tan\left(\frac{A}{2}\right)+A\right.\\ &\left.\left.-\sqrt{m+1}\left(2+\frac{A}{2}\cot\left(\frac{A}{2}\right)\right)\right)\right)^{-1} = P_{\text{load}}\end{aligned} \tag{36}$$

---

unknown variables from (10) results in the expression shown in (36), where $A = \frac{t_1}{\sqrt{L_r C_r}}$ and $T = \frac{\frac{1}{2f_{\text{sw}}}-t_1}{\sqrt{(L_r+L_m)C_r}}$. Since the equation presented in (36) is rather long and difficult to read in its present form, it can be split into different parts, as can be observed in (11) and (13).

REFERENCES

[1] B. Agrawal, M. Preindl, B. Bilgin, and A. Emadi, "Estimating switching losses for SiC MOSFETs with non-flat miller plateau region," in *Proc. IEEE Appl. Power Electron. Conf. Expo.*, Mar. 2017, pp. 2664–2670.

[2] P. G. Neudeck, R. S. Okojie, and L.-Y. Chen, "High-temperature electronics—A role for wide bandgap semiconductors?," *Proc. IEEE*, vol. 90, no. 6, pp. 1065–1076, Jun. 2002.

[3] D. Czarkowski and M. K. Kazimierczuk, "Phase-controlled *CLL* resonant converter," in *Proc. 8th Annu. Appl. Power Electron. Conf. Expo.*, Mar. 1993, pp. 432–438.

[4] M. K. Kazimierczuk and T. Nandakumar, "Class D voltage-switching inverter with tapped resonant inductor," *IEE Proc. B – Elect. Power Appl.*, vol. 140, no. 3, pp. 177–185, May 1993.

[5] G. Yang, P. Dubus, and D. Sadarnac, "Double-phase high-efficiency, wide load range high-voltage/low-voltage *LLC* dc/dc converter for electric/hybrid vehicles," *IEEE Trans. Power Electron.*, vol. 30, no. 4, pp. 1876–1886, Apr. 2015.

[6] F. Musavi, M. Craciun, D. S. Gautam, W. Eberle, and W. G. Dunford, "An *LLC* resonant dc-dc converter for wide output voltage range battery charging applications," *IEEE Trans. Power Electron.*, vol. 28, no. 12, pp. 5437–5445, Dec. 2013.

[7] C. Duan, H. Bai, W. Guo, and Z. Nie, "Design of a 2.5-kW 400/12-V high-efficiency dc/dc converter using a novel synchronous rectification control for electric vehicles," *IEEE Trans. Transp. Electrific.*, vol. 1, no. 1, pp. 106–114, Jun. 2015.

[8] C. C. Hua, Y. H. Fang, and C. W. Lin, "*LLC* resonant converter for electric vehicle battery chargers," *IET Power Electron.*, vol. 9, no. 12, pp. 2369–2376, 2016.

[9] H. Wang, S. Dusmez, and A. Khaligh, "Design and analysis of a full-bridge *LLC*-based PEV charger optimized for wide battery voltage range," *IEEE Trans. Veh. Technol.*, vol. 63, no. 4, pp. 1603–1613, May 2014.

[10] D. Fu, Y. Liu, F. C. Lee, and M. Xu, "A novel driving scheme for synchronous rectifiers in *LLC* resonant converters," *IEEE Trans. Power Electron.*, vol. 24, no. 5, pp. 1321–1329, May 2009.

[11] X. Sun, Y. Shen, Y. Zhu, and X. Guo, "Interleaved boost-integrated *LLC* resonant converter with fixed-frequency PWM control for renewable energy generation applications," *IEEE Trans. Power Electron.*, vol. 30, no. 8, pp. 4312–4326, Aug. 2015.

[12] S. M. Tayebi, H. Hu, O. Abdel-Rahman, and I. Batarseh, "Design and analysis of a dual-input single-resonant tank *LLC* converter for PV applications," in *Proc. IEEE Appl. Power Electron. Conf. Expo.*, Mar. 2018, pp. 476–483.

[13] S. Di Mauro, S. Musumeci, A. Raciti, F. Fusillo, F. Scrimizzi, and R. Scollo, "Synchronous rectification with low voltage MOSFETs in *LLC* converters," in *Proc. AEIT Int. Annu. Conf.*, Sep. 2017, pp. 1–6.

[14] Y. S. Cheng, J. H. Chen, Y. H. Liu, K. L. Huang, and Z. Z. Yang, "Design of a digitally-controlled *LLC* resonant converter with synchronous rectification," in *Proc. 1st Int. Future Energy Electron. Conf.*, Nov. 2013, pp. 772–776.

[15] C. Zheng, B. Chen, L. Zhang, R. Chen, and J. S. Lai, "Design considerations of *LLC* resonant converter for contactless laptop charger," in *Proc. IEEE Appl. Power Electron. Conf. Expo.*, Mar. 2015, pp. 3341–3347.

[16] W. Feng, F. C. Lee, and P. Mattavelli, "Optimal trajectory control of burst mode for *LLC* resonant converter," *IEEE Trans. Power Electron.*, vol. 28, no. 1, pp. 457–466, Jan. 2013.

[17] C. Buccella, C. Cecati, H. Latafat, P. Pepe, and K. Razi, "Observer-based control of *LLC* dc/dc resonant converter using extended describing functions," *IEEE Trans. Power Electron.*, vol. 30, no. 10, pp. 5881–5891, Oct. 2015.

[18] H. P. Park and J. H. Jung, "PWM and PFM hybrid control method for *LLC* resonant converters in high switching frequency operation," *IEEE Trans. Ind. Electron.*, vol. 64, no. 1, pp. 253–263, Jan. 2017.

[19] M. Mohammadi and M. Ordonez, "Extreme start-up response of *LLC* converters using average geometric control," in *Proc. IEEE Energy Convers. Congr. Expo.*, Sep. 2016, pp. 1–7.

[20] C. O. Yeon, J. W. Kim, M. H. Park, I. O. Lee, and G. W. Moon, "Improving the light-load regulation capability of *LLC* series resonant converter using impedance analysis," *IEEE Trans. Power Electron.*, vol. 32, no. 9, pp. 7056–7067, Sep. 2017.

[21] X. Wu, H. Chen, and Z. Qian, "1-MHz *LLC* resonant dc transformer (dcx) with regulating capability," *IEEE Trans. Ind. Electron.*, vol. 63, no. 5, pp. 2904–2912, May 2016.

[22] W. Feng, F. C. Lee, P. Mattavelli, and D. Huang, "A universal adaptive driving scheme for synchronous rectification in *LLC* resonant converters," *IEEE Trans. Power Electron.*, vol. 27, no. 8, pp. 3775–3781, Aug. 2012.

[23] J. Zhang, J. Wang, G. Zhang, and Z. Qian, "A hybrid driving scheme for full-bridge synchronous rectifier in *LLC* resonant converter," *IEEE Trans. Power Electron.*, vol. 27, no. 11, pp. 4549–4561, Nov. 2012.

[24] Y. Gu, Z. Lu, L. Hang, Z. Qian, and G. Huang, “Three-level *LLC* series resonant dc/dc converter,” *IEEE Trans. Power Electron.*, vol. 20, no. 4, pp. 781–789, Jul. 2005.

[25] K. Jin and X. Ruan, “Hybrid full-bridge three-level *LLC* resonant converter—A novel dc-dc converter suitable for fuel-cell power system,” *IEEE Trans. Ind. Electron.*, vol. 53, no. 5, pp. 1492–1503, Oct. 2006.

[26] R. Beiranvand, B. Rashidian, M. R. Zolghadri, and S. M. H. Alavi, “Using *LLC* resonant converter for designing wide-range voltage source,” *IEEE Trans. Ind. Electron.*, vol. 58, no. 5, pp. 1746–1756, May 2011.

[27] R. Yu, G. K. Y. Ho, B. M. H. Pong, B. W. Ling, and J. Lam, “Computer-aided design and optimization of high-efficiency *LLC* series resonant converter,” *IEEE Trans. Power Electron.*, vol. 27, no. 7, pp. 3243–3256, Jul. 2012.

[28] F. Musavi, M. Craciun, M. Edington, W. Eberle, and W. G. Dunford, “Practical design considerations for a *LLC* multi-resonant dc-dc converter in battery charging applications,” in *Proc. 27th Annu. IEEE Appl. Power Electron. Conf. Expo.*, Feb. 2012, pp. 2596–2602.

[29] S. D. Johnson and R. W. Erickson, “Steady-state analysis and design of the parallel resonant converter,” *IEEE Trans. Power Electron.*, vol. 3, no. 1, pp. 93–104, Jan. 1988.

[30] I. Batarseh, R. Liu, A. Ortiz-Conde, A. Yacoub, and K. Siri, “Steady state analysis and performance characteristics of the *LLC*-type parallel resonant converter,” in *Proc. 25th Annu. IEEE Power Electron. Spec. Conf.*, Jun. 1994, vol. 1, pp. 597–606.

[31] A. F. Wittulski and R. W. Erickson, “Steady-state analysis of the series resonant converter,” *IEEE Trans. Aerosp. Electron. Syst.*, vol. AES-21, no. 6, pp. 791–799, Nov. 1985.

[32] S. G. Trabert and R. W. Erickson, “Steady state analysis of the duty cycle controlled series resonant converter,” in *Proc. IEEE Power Electron. Spec. Conf.*, Jun. 1987, pp. 545–556.

[33] B. Y. Luan, S. Hu, Y. F. Zhang, and X. Li, “Steady-state analysis of a series resonant converter with modified PWM control,” in *Proc. 12th IEEE Conf. Ind. Electron. Appl.*, Jun. 2017, pp. 1143–1148.

[34] H.-J. Jiang, G. Maggetto, and P. Lataire, “Steady-state analysis of the series resonant dc-dc converter in conjunction with loosely coupled transformer-above resonance operation,” *IEEE Trans. Power Electron.*, vol. 14, no. 3, pp. 469–480, May 1999.

[35] J. F. Lazar and R. Martinelli, “Steady-state analysis of the *LLC* series resonant converter,” in *Proc. 16th Annu. IEEE Appl. Power Electron. Conf. Expo. (Cat. No.01CH37181)*, 2001, vol. 2, pp. 728–735.

[36] X. Li and A. K. Rathore, “Steady-state analysis of a dual-bridge *LLC* inverter,” in *Proc. 7th IEEE Conf. Ind. Electron. Appl.*, Jul. 2012, pp. 769–774.

[37] Z. Fang, S. Duan, C. Chen, X. Chen, and J. Zhang, “Optimal design method for *LLC* resonant converter with wide range output voltage,” in *Proc. 28th Annu. IEEE Appl. Power Electron. Conf. Expo.*, Mar. 2013, pp. 2106–2111.

[38] W. Liu, B. Wang, W. Yao, Z. Lu, and X. Xu, “Steady-state analysis of the phase shift modulated *LLC* resonant converter,” in *Proc. IEEE Energy Convers. Congr. Expo.*, Sep. 2016, pp. 1–5.

[39] Y. Shen, H. Wang, F. Blaabjerg, X. Sun, and X. Li, “Analytical model for *LLC* resonant converter with variable duty-cycle control,” in *Proc. IEEE Energy Convers. Congr. Expo.*, Sep. 2016, pp. 1–7.

[40] N. Mohan, T. M. Undeland, and W. P. Robbins, *Power Electronics: Converters, Applications and Design*, 3rd ed. Hoboken, NJ, USA: Wiley, 2003.

[41] M. K. Kazimierczuk and D. Czarkowski, *Resonant Power Converters*, 2nd ed. Hoboken, NJ, USA: Wiley, 2011.

[42] N. Shafiei, M. A. Saket, and M. Ordonez, “Time domain analysis of *LLC* resonant converters in the boost mode for battery charger applications,” in *Proc. IEEE Energy Convers. Congr. Expo.*, Oct. 2017, pp. 4157–4162.

[43] E. S. Glitz, M. Amyotte, M. C. G. Perez, and M. Ordonez, “*LLC* converters: Beyond datasheets for MOSFET power loss estimation,” in *Proc. IEEE Appl. Power Electron. Conf. Expo.*, Mar. 2018, pp. 464–468.

[44] G. Hua and F. C. Lee, “Soft-switching techniques in PWM converters,” *IEEE Trans. Ind. Electron.*, vol. 42, no. 6, pp. 595–603, Dec. 1995.

[45] B. Yang, F. C. Lee, A. J. Zhang, and G. Huang, “*LLC* resonant converter for front end dc/dc conversion,” in *Proc. 17th Annu. IEEE Appl. Power Electron. Conf. Expo. (Cat. No.02CH37335)*, 2002, vol. 2, pp. 1108–1112.

[46] J. W. Kolar, H. Ertl, and F. C. Zach, “How to include the dependency of the RDS(on) of power MOSFETs on the instantaneous value of the drain current into the calculation of the conduction losses of high-frequency three-phase PWM inverters,” *IEEE Trans. Ind. Electron.*, vol. 45, no. 3, pp. 369–375, Jun. 1998.

[47] Y. Ren, M. Xu, J. Zhou, and F. C. Lee, “Analytical loss model of power MOSFET,” *IEEE Trans. Power Electron.*, vol. 21, no. 2, pp. 310–319, Mar. 2006.

[48] M. Rodriguez, A. Rodriguez, P. F. Miaja, D. G. Lamar, and J. S. Zniga, “An insight into the switching process of power MOSFETs: An improved analytical losses model,” *IEEE Trans. Power Electron.*, vol. 25, no. 6, pp. 1626–1640, Jun. 2010.

[49] J. Fu, Z. Zhang, Y. F. Liu, and P. C. Sen, “MOSFET switching loss model and optimal design of a current source driver considering the current diversion problem,” *IEEE Trans. Power Electron.*, vol. 27, no. 2, pp. 998–1012, Feb. 2012.

[50] *IPZ60R040C7 Power Transistor Datasheet v. 2.0*, Infineon Technologies AG, Neubiberg, Germany, 2008.

[51] C. Xiao, G. Chen, and W. G. H. Odendaal, “Overview of power loss measurement techniques in power electronics systems,” *IEEE Trans. Ind. Appl.*, vol. 43, no. 3, pp. 657–664, May 2007.

[52] *Primary Side MOSFET Selection for LLC Topology v. 1.0*, Infineon Technologies AG, Neubiberg, Germany, 2014.

[53] *Half Bridge Resonant LLC Converters and Primary Side MOSFET Selection, Rev. 1*, STMicroelectronics, Geneva, Switzerland, 2015.

[54] *MOSFET Power Losses Calculation Using the Data-Sheet Parameters* v. 1.1, Infineon Technologies AG, Neubiberg, Germany, 2006.

Ettore Scabeni Glitz (S’17) was born in Curitiba, Brazil. He received the B.Eng. degree in electrical engineering from the Federal University of Technology – Parana, Curitiba, Brazil, and the M.A.Sc. degree in electrical and computer engineering from The University of British Columbia, Vancouver, BC, Canada, in 2016 and 2019, respectively.

He is currently an Electrical Designer with AES Engineering, Vancouver, BC, Canada.

Martin Ordonez (S’02–M’09) was born in Neuquen, Argentina. He received the Ing. degree in electronics engineering from the National Technological University, Cordoba, Argentina, and the M.Eng. and Ph.D. degrees in electrical engineering from the Memorial University of Newfoundland (MUN), St. Johns, NL, Canada, in 2003, 2006, and 2009, respectively.

He was an Adjunct Professor with Simon Fraser University, Burnaby, BC, Canada, and MUN. He is currently a Professor and Canada Research Chair in Power Converters for Renewable Energy Systems with the Department of Electrical and Computer Engineering, The University of British Columbia, Vancouver, BC, Canada. He is also the holder of the Fred Kaiser Professorship on Power Conversion and Sustainability at UBC. His industrial experience in power conversion includes research and development at Xantrex Technology Inc./Elgar Electronics Corp. (now AMETEK Programmable Power in San Diego, California). With the support of industrial funds and the Natural Sciences and Engineering Research Council, he has contributed to more than 150 publications and R&D reports.

Dr. Ordonez is a Guest Editor for IEEE Journal of Emerging and Selected Topics in Power Electronics, Associate Editor of the IEEE Transactions on Power Electronics, and Editor for IEEE Transactions on Sustainable Energy. He serves on several IEEE committees, and reviews widely for IEEE/IET journals and international conferences. He is the recipient of the David Dunsiger Award for Excellence in the Faculty of Engineering and Applied Science (2009) and the Chancellors Graduate Award/Birks Graduate Medal (2006), and became a Fellow of the School of Graduate Studies, MUN.